Onset of Turbulence in a Pipe

L. Boberg and U. Brosa

Fachbereich Physik der Philipps-Universität, Marburg

Z. Naturforsch. **43a**, 697–726 (1988); received June 15, 1988

Turbulence in a pipe is derived directly from the Navier-Stokes equation. Analysis of numerical simulations revealed that small disturbances called 'mothers' induce other much stronger disturbances called 'daughters'. Daughters determine the look of turbulence, while mothers control the transfer of energy from the basic flow to the turbulent motion. From a practical point of view, ruling mothers means ruling turbulence. For theory, the mother-daughter process represents a mechanism permitting chaotic motion in a linearly stable system. The mechanism relies on a property of the linearized problem according to which the eigenfunctions become more and more collinear as the Reynolds number increases. The mathematical methods are described, comparisons with experiments are made, mothers and daughters are analyzed, also graphically, with full particulars, and the systematic construction of small systems of differential equations to mimic the non-linear process by means as simple as possible is explained. We suggest that more then 20 but less than 180 essential degrees of freedom take part in the onset of turbulence.

PACS number: 47.25. Ae

1. Even the Most Ordinary Things are not Understood

The reason for turbulence in a pipe remained obscure for more than one hundred years counted from the first clear statement of the problem [1] although the importance of the question was generally recognized. The pecularity of pipe flow consists in its linear stability. If one divides the total velocity field

$$\boldsymbol{U}(\boldsymbol{r}, t) = \boldsymbol{U}_{\mathrm{HP}}(r) + \boldsymbol{u}(\boldsymbol{r}, t) \tag{1}$$

into the basic Hagen-Poiseuille flow $\boldsymbol{U}_{\mathrm{HP}}(r)$ and a disturbance $\boldsymbol{u}(\boldsymbol{r}, t)$, it turns out that all sufficiently small disturbances go to zero as time t goes to infinity no matter how large the flow velocity might be. This is different with all the other hydrodynamic systems which, up to now, have been investigated, e.g. with the Rayleigh-Bénard and Taylor systems, or with channel and boundary-layer flow [2]. In all these cases, linear instability prevents final calming; the non-linearity just causes irregularities and prohibits thus infinite growth of the disturbance. In other words: It takes energy to sustain turbulence, and this energy usually migrates from the basic flow to the disturbance via a linear instability. For pipe flow, however, the energy supply has to work differently.

Reprint requests to Dr. U. Brosa, HLRZ/KFA-Jülich, Postfach 19 13, D-5170 Jülich, FRG.

It might seem that pipe flow constitutes an exceptional problem. But this is not true: Channel and boundary-layer flows are often turbulent at so small Reynolds numbers that a linear instability can't be present [3]. Hence, as soon as we understand the onset of turbulence in the pipe, we have a chance to understand what is called 'subcritical transition' in other shear flows, and to establish a model for the onset of chaos in systems without linear instability.

In this paper we present a study on the onset of turbulence in a pipe. It is a derivation directly from the Navier-Stokes equation. We used numerical methods but could reduce the results to so simple terms that some pictures and a little bit analysis suffice to make a significant part of the mechanism understandable. Figure 1 symbolizes the outcome of our investigation. Let us split the disturbance $\boldsymbol{u}(\boldsymbol{r}, t) = \boldsymbol{u}_{\mathrm{T}}(\boldsymbol{r}, t) + \boldsymbol{u}_{\mathrm{M}}(\boldsymbol{r}, t)$ into two flow systems, called 'daughters' $\boldsymbol{u}_{\mathrm{T}}(\boldsymbol{r}, t)$ and 'mothers' $\boldsymbol{u}_{\mathrm{M}}(\boldsymbol{r}, t)$, and let us first discuss the effects of linearity. The daughters usually own and dissipate almost all energy. But a pure society of daughters would quickly become extinct. They need another flow system, the mothers, to get fed. The mothers, mostly weak currents, have access to the energy of the basic flow but cannot incorporate it for their own benefit. As a consequence we find a strong increase of turbulent energy as long as the mothers exist. But when the mothers are gone, the daughters fade also. This is the situation where the non-linearity becomes

0932-0784 / 88 / 0800-0679 $ 01.30/0. – Please order a reprint rather than making your own copy.

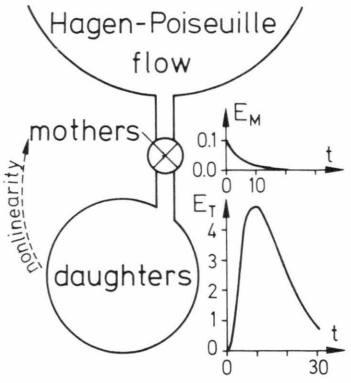

Fig. 1. The mother-daughter mechanism. At the top of the picture we symbolize the Hagen-Poiseuille flow as an infinite reservoir of energy (which is practically provided by the pumps). From the Hagen-Poiseuille flow the energy is conducted to the turbulence-featuring daughters. The nearly invisible, since small mothers, however, control the access to energy. The graphs on the right-hand side display the energies E_M and E_T of mothers and daughters as functions of time t. The numbers have the correct order of magnitude for pipe flow: The daughters typically get about ten times more energy than the mothers; the lifetime of daughters is usually not more than three times longer than that of the mothers.

effective. It transforms part of the daughters into mothers, and the whole play may start again. It must be stressed that it is a linear mechanism that provides the turbulence with energy, despite of the linear stability. The non-linearity is of outmost importance for the permanence of the process, but it acts essentially without access to power.

The following chapters are to develop this outline. The analytical and numerical methods are expounded in Chapter 2. The results of the full-fledged computer simulations can be found in Chapt. 3, where also a preliminary comparison with observables is given. Chapter 4 contains the analysis of these results in terms of the mother-daughter mechanism. Although its non-linear part is indispensable, we found that it does not need to have very special properties. It seems to be special in so far as it takes many degrees of freedom to become effective. The respective arguments are presented in Chapter 5. Finally, in Chapt. 6, the experimentalists are urged to verify the physical picture; we point to the things that one should be able to see.

As a conclusion of this introduction it is a pleasure to mention previous work that we found useful for our studies. Many references concerning the linear stability of pipe flow can be found in Drazin and Reid's book [2]. Lessen, Saddler, and Liu [4], in particular, underlined the necessity to look for disturbances without axial symmetry. Burridge and Drazin [5] first stressed the usefulness of certain eigenfunctions which we call Stokes functions (see Sect. 2.1 and the Appendix). Furthermore, they derived their results from the vorticity equation (called in their paper Sexl's equation), and this is much better than a start from the Navier-Stokes equation without proper elimination of the pressure, as done e.g. by Salwen, Grosch and Cotton [6]. Probably Davey and Nguyen [7] made the first attempt to found a non-linear theory of pipe-flow stability. They obtained a limit for the amplitude of a certain disturbance beyond which they expected instability. Their calculations were extended by Sen et al. [8]. All these authors used Landau theory. Itoh, however, suggested that the application of Landau theory to pipe flow might not be justified since Landau theory needs the vicinity of a linear instability [9]. Later on Patera and Orszag [10] confirmed Itoh's suggestion by numerical simulations, and so do we: There is no non-linear instability of the kind imagined by Davey and Nguyen. Another interesting approach was the application of non-linear boundary-layer theory by Smith and Bodonyi [11]. In contrast to Davey and Nguyen [7], these authors found that the onset of turbulence should be caused by a non-axisymmetric disturbance, and so do we (Sect. 2.3, 3.2, and 4.1): Patera and Orszag [10] failed to discover the turbulence because their algorithms were restricted to axial symmetry. But there is still another catch. All the investigations based on Landau and non-linear boundary-layer theories aimed just at the calculation of stationary waves. The idea was that these waves should be regarded as unstable limit cycles which separate the basins of laminar and turbulent flow. We thought it would be too risky to start with such a restriction and, as a matter of fact, saw never the slightest indication of those waves in our results. In summary, our theory is more general than previous approaches because we simultaneously take non-linear interactions into account, admit disturbances without axial symmetry, and do not presume any special dependence on time.

References regarding experimental work will be given in the Sect. 3.1, 3.2, and 6.

2. Mathematical Methods

This chapter is mainly concerned with handicraft and instrumentation. But an analysis of tools reveals

also some points of physical significance:

α) Usage of Stokes modes permits to build the dynamics on the vorticity equation. The pressure is thus properly eliminated from the equations of motion.

β) Without recourse to numerical calculations one can see that turbulence in a pipe subsists on energy transfer by a linear mechanism.

γ) Without recourse to numerical calculations one can see that the most important modes for turbulence are certain non-axisymmetric ones ($m = \pm 1$). Modes with axial symmetry ($m = 0$) must just take part as mediators to allow non-linear coupling.

δ) The equations of motion that we take for numerical treatment are essentially not stiff.

2.1 Derivation of the Galerkin Equations

We start from the Navier-Stokes equation

$$\partial_t \boldsymbol{U} + (\boldsymbol{U}\boldsymbol{\nabla})\,\boldsymbol{U} = -\boldsymbol{\nabla}P - 1/\mathrm{Re}\;\boldsymbol{\nabla}\times\boldsymbol{\nabla}\times\boldsymbol{U} \qquad (2)$$

and use units which express the velocities $\boldsymbol{U}(\boldsymbol{r},t)$ as multiples of the velocity U_0 of the Hagen-Poiseuille flow at the pipe's center, pressures $P(\boldsymbol{r},t)$ as multiples of $\varrho_0 U_0^2$, ϱ_0 denoting the mass density, lengths or positions $\boldsymbol{r}$ in terms of the pipe's radius R_0, and times t as multiples of R_0/U_0. The Reynolds number is as customary defined by $\mathrm{Re} := U_0 R_0/\nu_0$, ν_0 denoting the kinematic viscosity. As we deal with incompressible fluids ($\boldsymbol{\nabla}\boldsymbol{U} = 0$), the Navier-Stokes equation is just good enough to compute the pressure by a contour integration

$$P(\boldsymbol{r},t) = -\int (\partial_t \boldsymbol{U} + (\boldsymbol{U}\boldsymbol{\nabla})\,\boldsymbol{U} + 1/\mathrm{Re}\;\boldsymbol{\nabla}\times\boldsymbol{\nabla}\times\boldsymbol{U})\,\mathrm{d}\boldsymbol{r} \qquad (3)$$

from the velocity field $\boldsymbol{U}(\boldsymbol{r},t)$. Since the integrand, from the Navier-Stokes equation, is a gradient, the integral (3) does not depend on the contour. Hence the curl of the integrand must be zero. This gives the vorticity equation

$$\partial_t \boldsymbol{W} = \boldsymbol{\nabla}\times(\boldsymbol{U}\times\boldsymbol{W}) - 1/\mathrm{Re}\;\boldsymbol{\nabla}\times\boldsymbol{\nabla}\times\boldsymbol{W}. \qquad (4)$$

$\boldsymbol{W} := \boldsymbol{\nabla}\times\boldsymbol{U}$ defines the vorticity. The pressure is thus eliminated, but at first sight it appears as if we had just traded the pressure for the vorticity; it does not seem easier to close the vorticity equation (4) than to treat immediately the Navier-Stokes equation (2). For two-dimensional flows this difficulty is solved by the introduction of a stream function [2]. For three-dimensional problems we proceed as follows: The velocity field $\boldsymbol{U}(\boldsymbol{r},t) = \sum_{\nu=0}^{N} a_\nu(t)\,\boldsymbol{u}_\nu(\boldsymbol{r})$ is expanded in terms of certain vector functions $\boldsymbol{u}_\nu(\boldsymbol{r})$ which all, piece by piece, satisfy the boundary conditions and have zero divergence. When we take the curl, we see that the vorticity is uniquely determined from the velocity field as $\boldsymbol{W} = \sum a_\nu(\boldsymbol{\nabla}\times\boldsymbol{u}_\nu)$. But also the opposite is true: From $\boldsymbol{W} = \sum a_\nu \boldsymbol{w}_\nu$ the velocity field is uniquely determined as $\boldsymbol{U} = \sum a_\nu \boldsymbol{u}_\nu$ if $\boldsymbol{w}_\nu = \boldsymbol{\nabla}\times\boldsymbol{u}_\nu$. This holds because a vector field is fixed if its divergence, its curl, and its boundary values are given.

To be definite: As the dynamic equation we take the vorticity equation (4) with boundary conditions for the velocity field

$$\boldsymbol{U}(r=1,\varphi,z,t) = 0 \qquad (5)$$

and

$$\boldsymbol{U}(r,\varphi,z+L,t) = \boldsymbol{U}(r,\varphi,z,t), \qquad (6)$$

i.e. the velocity is zero on the walls, and the flow is assumed periodic along the pipe's axis. The vector of position $\boldsymbol{r}$ is expressed here in cylindrical coordinates (r,φ,z). We solve the vorticity equation by the ansatz

$$\boldsymbol{U}(\boldsymbol{r},t) = \boldsymbol{U}_{\mathrm{HP}}(r) + \sum_{\nu=1}^{N} a_\nu(t)\,\boldsymbol{s}_\nu(\boldsymbol{r}) \qquad (7)$$

for $0 \le r < 1$, $0 \le \varphi < 2\pi$, $0 \le z < L$.

Its first constituent is the Hagen-Poiseuille flow

$$\boldsymbol{U}_{\mathrm{HP}}(r) := (1-r^2)\,\boldsymbol{e}_z, \qquad (8)$$

which depends only on the radial coordinate r and points everywhere into the direction of the pipe's axis described by the unit vector $\boldsymbol{e}_z$. Obviously, Hagen-Poiseuille flow is free from divergence and fulfils the boundary conditions (5) and (6).

The other constituents of (7) are the 'Stokes functions' $\boldsymbol{s}_\nu(\boldsymbol{r})$ which satisfy Stokes' differential equation

$$-\alpha_\nu^2\,\boldsymbol{s}_\nu = -\boldsymbol{\nabla}p_\nu - \boldsymbol{\nabla}\times\boldsymbol{\nabla}\times\boldsymbol{s}_\nu, \qquad (9)$$

have zero divergence and obey the same boundary conditions (5) and (6) as the total velocity field does. These properties define a self-adjoint problem of the Sturm-Liouville type. Equation (9) is nothing else than the Navier-Stokes equation for very slow flow, written as an eigenvalue problem. The functions $p_\nu(\boldsymbol{r})$ have therefore only for very slow motion the meaning of pressures. Here it is only important to state that they are scalar functions. The eigenfunctions have the structure

$$\boldsymbol{s}_\nu(\boldsymbol{r}) = \boldsymbol{S}_{n,m,l}(r)\,e^{i(m\varphi+\beta z)}, \qquad \beta \equiv 2\pi l/L. \qquad (10)$$

The vectors $\boldsymbol{S}_{n,m,l}(r)$ describe the radial behavior. They guarantee the observance of the boundary condition (5) while the radial node index takes the values $n = 1, 2, \ldots$. The azimuthal node index or the 'multipolarity' is restricted to the values $m = 0, \pm 1, \pm 2, \ldots$ to secure the uniqueness of the Stokes functions. Because of the boundary condition (6), the axial node index must be an integer $l = 0, \pm 1, \pm 2, \ldots$. Every Stokes function is thus labelled by three indices which we abbreviate by one greek letter, $\nu \triangleq (n, m, l)$ or, if necessary, more precisely by $\nu \triangleq (n_\nu, m_\nu, l_\nu)$. The eigenvalues $\alpha_\nu^2 = \alpha_{n,m,l}^2$ are positive. Considered as functions of n, i.e. for each fixed m and l, they behave for large n as n^2. All the properties of the Stokes functions can be obtained by classical analysis; numerical means are necessary only for the final evaluation. The respective formulas are listed in the Appendix.

The Stokes functions have the amazing property of double orthogonality: The usual orthogonality follows immediately from the self-adjointness of the problem

$$\int_{(\text{pipe})} \boldsymbol{s}_\mu^* \, \boldsymbol{s}_\nu \, \mathrm{d}\tau = \delta_{\mu\nu}. \tag{11}$$

The spatial integration extends over the periodicity volume of the pipe. With this normalization we obtain from (9) and from the rules of field theory another orthogonality

$$\int_{(\text{pipe})} \boldsymbol{w}_\mu^* \, \boldsymbol{w}_\nu \, \mathrm{d}\tau = \alpha_\mu^2 \, \delta_{\mu\nu}, \tag{12}$$

namely for the 'Stokes vorticities' $\boldsymbol{w}_\nu(\boldsymbol{r}) := \boldsymbol{\nabla} \times \boldsymbol{s}_\nu(\boldsymbol{r})$. The simultaneous validity of both relations, (11) and (12), eased all further work considerably.

We take now the expansion (7) and insert it into the vorticity equation (4). Then we multiply this with the complex conjugate Stokes vorticities $\boldsymbol{w}_\mu^*(\boldsymbol{r})$, integrate, and use the orthogonality relations (12). This results in a system of ordinary differential equations for the amplitudes $a_\mu(t)$,

$$\begin{aligned} d_t \, a_\mu(t) = {} & W_\mu^{\varkappa\lambda} \, a_\varkappa(t) \, a_\lambda(t) + H_\mu^\varkappa \, a_\varkappa(t) \\ & + 1/\mathrm{Re} \; D_\mu^\varkappa \, a_\varkappa(t), \end{aligned} \tag{13}$$

where $\varkappa$, λ, and μ run from 1 to N, and sums go over $\varkappa$ and λ. These 'Galerkin equations' are the foundation for our numerical work.

The definitions of the matrix elements $W_\mu^{\varkappa\lambda}$, $H_\mu^\varkappa$, and $D_\mu^\varkappa$ follow from the derivation of (13). We give here slightly reformulated expressions:

$$W_\mu^{\varkappa\lambda} = \frac{1}{\alpha_\mu^2} \int_{(\text{pipe})} \boldsymbol{\nabla} \times \boldsymbol{w}_\mu^* (\boldsymbol{s}_\varkappa \times \boldsymbol{w}_\lambda) \, \mathrm{d}\tau, \tag{14}$$

$$H_\mu^\varkappa = \frac{1}{\alpha_\mu^2} \int_{(\text{pipe})} \boldsymbol{\nabla} \times \boldsymbol{w}_\mu^* (\boldsymbol{s}_\varkappa \times \boldsymbol{W}_{\mathrm{HP}} + \boldsymbol{U}_{\mathrm{HP}} \times \boldsymbol{w}_\varkappa) \, \mathrm{d}\tau, \tag{15}$$

$$D_\mu^\varkappa = -\alpha_\mu^2 \, \delta_\mu^\varkappa \tag{16}$$

with $\boldsymbol{W}_{\mathrm{HP}}(r) := \boldsymbol{\nabla} \times \boldsymbol{U}_{\mathrm{HP}}(r)$ as vorticity of the Hagen-Poiseuille flow. These expressions are, due to the structure of the Stokes functions, advantageous for further evaluation.

The matrix $W_\mu^{\varkappa\lambda}$ represents the interaction between the Stokes modes. Insertion of (10) into (14) shows that the integrations over φ and z can be done at once. They deliver 'selection rules' for the node indices m and l:

$$\begin{aligned} W_\mu^{\varkappa\lambda} = 0 \quad & \text{if} \quad m_\varkappa + m_\lambda \neq m_\mu \\ & \text{or} \quad l_\varkappa + l_\lambda \neq l_\mu. \end{aligned} \tag{17}$$

The same reasoning leads to selection rules for the 'Hagen' and the 'dissipation' matrices:

$$\begin{aligned} H_\mu^\varkappa = 0 \quad \text{and} \quad D_\mu^\varkappa = 0 \quad & \text{if} \quad m_\varkappa \neq m_\mu \\ & \text{or} \quad l_\varkappa \neq l_\mu. \end{aligned} \tag{18}$$

The Hagen matrix describes the coupling between basic flow and Stokes modes. Both the interaction and Hagen matrices have only imaginary elements as both stem from the convection term $\boldsymbol{\nabla} \times (\boldsymbol{U} \times \boldsymbol{W})$ in the vorticity equation (4). The dissipation matrix, however, is a real and diagonal matrix. It takes no additional work at all to evaluate the dissipation matrix; the interaction and Hagen matrices are reduced to simple integrals.

For further discussions one should keep in mind that both Hagen and dissipation matrices correspond to linear processes. Non-linearity is exclusively represented by the interaction matrix.

2.2 Energy Balance

Take the decomposition (1) of the total flow and insert it into the Navier-Stokes equation (2). Manipulation with some identities from field theory leads to an energy balance for the disturbance:

$$\begin{aligned} d_t \tfrac{1}{2} \int_{(\text{pipe})} \boldsymbol{u}^2 \, \mathrm{d}\tau = {} & - \int_{(\text{ends of pipe})} (p + \tfrac{1}{2}\boldsymbol{u}^2) \, \boldsymbol{u} \, \mathrm{d}\boldsymbol{a} \\ & - \int_{(\text{pipe})} \boldsymbol{u}((\boldsymbol{u}\boldsymbol{\nabla}) \, \boldsymbol{U}_{\mathrm{HP}} + (\boldsymbol{U}_{\mathrm{HP}} \boldsymbol{\nabla}) \, \boldsymbol{u}) \, \mathrm{d}\tau \\ & - 1/\mathrm{Re} \int_{(\text{pipe})} (\boldsymbol{\nabla} \times \boldsymbol{u})^2 \, \mathrm{d}\tau. \end{aligned} \tag{19}$$

$p(\boldsymbol{r}, t)$ denotes the pressure field without the contribution from the Hagen-Poiseuille flow. We call

$$\tilde{E}_{\text{dis}} := \tfrac{1}{2} \int_{(\text{pipe})} \boldsymbol{u}^2 \, \mathrm{d}\tau \tag{20}$$

'energy of the disturbance'. The first term on the right-hand side of (19) is the 'interaction input'

$$\tilde{W}_{\text{inp}} := - \int_{(\text{ends of pipe})} (p + \tfrac{1}{2}\boldsymbol{u}^2)\, \boldsymbol{u} \, \mathrm{d}\boldsymbol{a}. \tag{21}$$

That it is related to the disturbance's non-linear self-interaction, is clear for the contribution with the factor $\frac{1}{2}\boldsymbol{u}^2$. For the term with the factor p this follows from the representation (3) of the pressure; we will see in the next section that it is, in this context, only the contribution $(\boldsymbol{u}\boldsymbol{\nabla})\boldsymbol{u}$ in (3) which matters. The second term on the right-hand side of (19) is the 'Hagen input'

$$\tilde{H}_{\text{inp}} := - \int_{(\text{pipe})} \boldsymbol{u}((\boldsymbol{u}\boldsymbol{\nabla})\boldsymbol{U}_{\text{HP}} + (\boldsymbol{U}_{\text{HP}}\boldsymbol{\nabla})\boldsymbol{u}) \, \mathrm{d}\tau, \tag{22}$$

which describes the coupling to the basic flow. The 'dissipation input'

$$\tilde{D}_{\text{inp}} := -1/\text{Re} \int_{(\text{pipe})} (\boldsymbol{\nabla} \times \boldsymbol{u})^2 \, \mathrm{d}\tau \tag{23}$$

corresponds to the dissipation caused only by the disturbance.

Take now the expansion (7) of the disturbance and use the orthogonality relations (11). The energy of the disturbance is then

$$E_{\text{dis}} := \tfrac{1}{2} \sum_{\mu=1}^{N} |a_\mu(t)|^2. \tag{24}$$

This is not exactly equal to $\tilde{E}_{\text{dis}}$ because the expansion (7) gives, for a finite truncation number N and a periodicity length L which is smaller than that of the real pipe, just an approximation to the true solution of the Navier-Stokes equation. The 'inputs' are here

$$W_{\text{inp}} := \Re\left(\sum_{\mu=1}^{N} a_\mu^* \, W_\mu^{\varkappa\lambda} \, a_\varkappa \, a_\lambda \right), \tag{25}$$

$$H_{\text{inp}} := \Re\left(\sum_{\mu=1}^{N} a_\mu^* \, H_\mu^{\varkappa} \, a_\varkappa \right), \tag{26}$$

$$D_{\text{inp}} := -1/\text{Re} \sum_{\mu=1}^{N} \alpha_\mu^2 \, |a_\mu|^2. \tag{27}$$

$\Re$ means real part, and only sums over μ are explicitly noted. With these definitions we obtain from the Galerkin equations (13) an energy balance:

$$d_t \, E_{\text{dis}} = W_{\text{inp}} + H_{\text{inp}} + D_{\text{inp}}, \tag{28}$$

which is the analog of (19).

The lesson to be learned from the juxtaposition of these two ways to write more or less the same energy balance concerns the interaction input. If we have a disturbance which is spacially periodic as in the expansion (7), the contributions from $\frac{1}{2}\boldsymbol{u}^2\,\boldsymbol{u}$ in (21) must cancel. Furthermore one might guess that the contribution from $p\boldsymbol{u}$ in (21) should also be zero since a periodic velocity field is expected to induce a periodic field of pressures. This, however, is wrong as will be demonstrated in the next section. And yet, $\tilde{W}_{\text{inp}}$ has contributions only from two small surfaces; in a closed system it even vanishes for all sorts of disturbances. $\tilde{H}_{\text{inp}}$ and $\tilde{D}_{\text{inp}}$, in contrast, describe processes in the volume. One is therefore entitled to assume that the interaction input is generally much smaller than the Hagen or dissipation inputs. And it seems to be reasonable to attribute the same relation to the respective quantities without tilde. The latter assumption will be confirmed by the numerical simulations to be presented in Section 3.3. It is nevertheless remarkable that familiar analysis alone indicates that turbulence gets its energy via linear interactions even if there is no instability without non-linearity.

2.3 The Pressure

There is not the least difficulty to obtain a general expression for the pressure that can be evaluated if the amplitudes $a_\mu(t)$ are known. One just has to insert the velocity (7) into the representation (3) and to use the formulas (A. 3–4) from the Appendix. But one may learn more from a special case.

Measurements with Pitot pipes or transducers inside the pipe are of course most valuable. But this is not what is presented in textbooks to explain the fundamental properties of pipe flow. There one finds figures to demonstrate that the coefficient of resistance jumps when turbulence sets in (see Fig. 5 below). The determination of resistance requires measurements of the total flow and of the difference of the pressures between the ends of the pipe. This difference is usually read from the level of the fluid in the source tank or from another quantity which is not strictly related to the pressure in the pipe. Nevertheless there is no doubt that for fixed total flow a large increase of the resistance can only happen if pressure grows in large portions of the pipe. In other words: If a theory is not able to yield a long-range growth of the pressure at the pipe's center, it has no chance to reproduce the classic jump effect in the resistivity.

To monitor long-range pressure growth, we studied the quantity

$$\Delta p(r,\varphi,t) := \frac{p(r,\varphi,z=L,t)-p(r,\varphi,z=0,t)}{L}, \qquad (29)$$

where $p(\boldsymbol{r},t) := P(\boldsymbol{r},t) - P_{\mathrm{HP}}(z)$ denotes pressure without contribution from Hagen-Poiseuille flow. Inspection of the Stokes modes reveals that those are rare for which the linear part in (3) already gives rise to $\Delta p \neq 0$: They are just the modes which do not depend on z. If none of these is included in the series (7), we obtain from (3)

$$\Delta p(r,\varphi,t) = -\frac{1}{L}\int_{(r,\varphi,z=0)}^{(r,\varphi,z=L)} (\boldsymbol{u}\nabla)\,\boldsymbol{u}\,\mathrm{d}\boldsymbol{r}. \qquad (30)$$

Even for spacially periodic disturbances $\boldsymbol{u}(\boldsymbol{r},t)$ with zero average this integral does not necessarily disappear since the integrand has generally a component independent of $\boldsymbol{r}$. If we insert now (7) and (10) and work the scalar product out with (A. 3 4), we find

$$\Delta p(r,\varphi,t) = -\Im \sum_{\varkappa}\sum_{\lambda} a_{\varkappa}(t)\,a_{\lambda}(t)\left\{u_{\varkappa}(r)\,\partial_r w_{\lambda}(r) - \frac{m_{\lambda}}{r} v_{\varkappa}(r)\,w_{\lambda}(r) - \beta_{\lambda}\,w_{\varkappa}(r)\,w_{\lambda}(r)\right\} e^{i(m_{\varkappa}+m_{\lambda})\varphi}\,\delta_{-l_{\varkappa}l_{\lambda}} \qquad (31)$$

with $\Im$ as sign for the imaginary part. The real functions $u_{\varkappa}(r)$, $v_{\varkappa}(r)$, and $w_{\varkappa}(r)$ are, apart from phase factors, the components of the Stokes functions in cylindrical coordinates.

We now specialize to the center of the pipe ($r = 0$). In this case Δp must not depend on the angle φ, and this generates another Kronecker symbol, namely $\delta_{-m_{\varkappa}m_{\lambda}}$ for the sum in (31). Furthermore, from (A. 4) follows that the expression in the curly brackets is different from zero only if both $|m_{\varkappa}|$ and $|m_{\lambda}|$ have values 0 or 1. The first term in these brackets is even identically zero. The third term does not contribute for the following reason: The sum in (31) is a fourfold one since $\varkappa$ corresponds to $(n_{\varkappa}, m_{\varkappa}, l_{\varkappa})$ and λ to $(n_{\lambda}, -m_{\varkappa}, -l_{\varkappa})$. Exchange of the indices $n_{\varkappa}$ and n_{λ}, and symmetrization transforms the third contribution in (31) into

$$-\tfrac{1}{2}\Im \sum_{n_{\varkappa}}\sum_{n_{\lambda}}\sum_{m_{\varkappa}}\sum_{l_{\varkappa}}\Bigg(a_{n_{\varkappa},m_{\varkappa},l_{\varkappa}}(t)\,a_{n_{\lambda},-m_{\varkappa},-l_{\varkappa}}(t)\,\frac{2\pi l_{\varkappa}}{L}\,w_{n_{\varkappa},m_{\varkappa},l_{\varkappa}}(0)\,w_{n_{\lambda},-m_{\varkappa},-l_{\varkappa}}(0) + a_{n_{\lambda},m_{\varkappa},l_{\varkappa}}(t)\,a_{n_{\varkappa},-m_{\varkappa},-l_{\varkappa}}(t)\,\frac{2\pi l_{\varkappa}}{L}\,w_{n_{\lambda},m_{\varkappa},l_{\varkappa}}(0)\,w_{n_{\varkappa},-m_{\varkappa},-l_{\varkappa}}(0)\Bigg). \qquad (32)$$

The flow (7) has to be a real field. This is save only if

$$a_{n,-m,-l}(t) = (-)^m a^*_{n,m,l}(t). \qquad (33)$$

The relation $w_{n,-m,-l}(r) = (-)^m w_{n,m,l}(r)$, on the other hand, is a property of the Stokes functions (cf. (A.15)). Both equations together permit to rewrite (32) as

$$-\tfrac{1}{2}\Im \sum_{n_{\varkappa}}\sum_{n_{\lambda}}\sum_{m_{\varkappa}}\sum_{l_{\varkappa}}\left(a_{n_{\varkappa},m_{\varkappa},l_{\varkappa}}(t)\,a^*_{n_{\lambda},m_{\varkappa},l_{\varkappa}}(t) + a^*_{n_{\varkappa},m_{\varkappa},l_{\varkappa}}(t)\,a_{n_{\lambda},m_{\varkappa},l_{\varkappa}}(t)\right)\frac{2\pi l_{\varkappa}}{L}\,w_{n_{\varkappa},m_{\varkappa},l_{\varkappa}}(0)\,w_{n_{\lambda},m_{\varkappa},l_{\varkappa}}(0), \qquad (34)$$

and this is nil since the sum is manifestly real. Hence we find as final simplification of (31)

$$\Delta p(r=0,t) = -\Im \sum_{n_{\varkappa}}\sum_{n_{\lambda}}\sum_{l_{\varkappa}}\sum_{m_{\varkappa}=-1}^{1} a_{n_{\varkappa},m_{\varkappa},l_{\varkappa}}(t)\,a_{n_{\lambda},-m_{\varkappa},-l_{\varkappa}}(t)\cdot\left[\frac{m_{\varkappa}}{r}\,v_{n_{\varkappa},m_{\varkappa},l_{\varkappa}}(r)\,w_{n_{\lambda},-m_{\varkappa},-l_{\varkappa}}(r)\right]_{r=0}. \qquad (35)$$

This formula shows that only non-axisymmetric modes ($m = \pm 1$) produce the large-scale pressure growth. The inclusion of these modes into the dynamic calculations is therefore mandatory. The modes with $m = \pm 1$ alone, however, cannot have non-linear interactions among themselves, as can be seen from the selection rules (17). Axisymmetric modes ($m = 0$) have to be built in for the sake of non-linearity.

By the way, with the same tricks as played in the derivation of (34) it is easy to prove that the pressure growth $\Delta p(r = 0, t)$ is zero if $n_{\varkappa}$ equals n_{λ}. The attempt to simulate turbulence with only one Stokes mode for each m and l is thus doomed to failure from the very start.

2.4 Numerics and Checks

For the use on vector computers a part of the code was rewritten [13] without, however, changing the algorithms. We applied only numerical methods with controlled accuracy. The following tasks were accomplished:

i) Standard and modified Bessel functions were computed as proposed by Press et al. [14, p. 171–180]. We always found an absolute accuracy of 10^{-8}.

ii) The characteristic equation (A.7) was solved with the Illinois algorithm [15]. This method needs for its start a lower and an upper bound which we took from (A.9). The Illinois algorithm keeps the true zero bracketed so that we knew that the relative accuracy was better than 10^{-7}.

iii) The interaction and Hagen matrices ((14) and (15)) were computed by Romberg integration with the Bulirsch sequence and extrapolation according to rational asymptotics [16]. The accuracy was not worse than 10^{-6}.

iv) The Galerkin equations (13), whose number ranged from 10 to 500 for the different cases, were solved by three different methods: a Runge-Kutta-Fehlberg procedure [17], the classic Bulirsch-Stoer procedure [16], and the semi-implicit Bader-Deuflhard method [18]. The self-controlled accuracy was always better than 10^{-6} per step; at most 10000 steps were done per run. The Bader-Deuflhard method was specifically developped for stiff equations, and large systems are usually stiff. Our Galerkin equations, however, turned out to be well-conditioned. This could be seen from the step-size controls of the Runge-Kutta-Fehlberg or Bulirsch-Stoer procedures which select automatically step sizes that are much too small as compared to the relative change of the solution when the differential equation becomes stiff. But we had mostly less than 10 steps per "oscillation" with the Bulirsch-Stoer procedure and less than 100 steps with the Runge-Kutta-Fehlberg routine. Of course, to nonlinear differential equations global stiffness cannot be attributed. They behave differently in different regions of the phase space. For example, the Galerkin equations (13) are stiff in the neighborhood of the initial conditions (37). Our routines remain accurate also in these regions. They just contract the step size and waste thus computational time. But the regions of stiffness are rarely visited. Consequently this waste is smaller than the waste caused by a routine for stiff equations which has to operate mostly in non-stiff regions. The Bader-Deuflhard method was thus not economical for our problem. The Bulirsch-Stoer procedure proved to be most effective especially for the turbulent motions. Therefore it was chosen to do most of the work.

v) To clarify the meaning of daughters and mothers, we had to solve the 'Hagen problem', i.e. the vorticity equation was linearized about the Hagen-Poiseuille solution, and the respective eigenvalues and eigenfunctions were found (cf. Section 4.3). This led to an algebraic eigenvalue problem with the symmetric dissipation and the asymmetric Hagen matrices (see (16) and (15)). The calculation went on as follows: balancing, reduction to Hessenberg form, and QR transformations [14, pp. 365–376]. Matrices with up to 70×70 complex elements were processed. The accuracy was not worse than that of the matrix elements, i.e. about 10^{-6}.

vi) In the quest of the ideal mother (Sect. 4.1) we had to maximize a function of typically twenty independent variables which was not very accurately known (error 10^{-2}). Hence we could not apply a procedure that implies analytic properties of that function. We took the Nelder-Mead algorithm [19]. The final accuracy was better than 10^{-1}.

vii) Determinants of large, ill-conditioned matrices (Sect. 4.4) were calculated by Gaussian elimination with search for the absolutely best pivot elements [16]. The obtained numbers were not used for further calculations or quantitative comparisons.

Most computing was done on 64-bit machines, but we checked that the results to be presented in the next chapters can be also obtained with a 32-bit machine.

The computation of the Stokes functions (item i and ii above) was checked, first, by graphical inspection of the nodal structure and the boundary conditions, second, by numerical examination of the orthonormality relations (11). This is a stringent test since also an analytical formula (A.12) is available for these integrals. Numerical and analytical results coincide only if the checked functions satisfy at the same time differential equation (9) and boundary conditions (5–6).

The interaction and Hagen integrals (item iii) were checked by rewriting the integrals (14) and (15) using the rules of field theory. In all cases we had at least two equivalent forms with different integrands. Numerical evaluation, however, yielded within the prescribed accuracy the same values.

The solutions of the Galerkin equations (13) (item iv) were found, as explained above, by three different procedures. For laminar runs, these routines gave the same results within the prescribed accuracy. For tur-

bulent runs, the results from the different routines diverged only after more than ten 'oscillations'. Such a behavior is typical and unavoidable in chaotic systems. Moreover, we checked item iv by reproducing all the results obtained by Patera and Orszag [10] for axisymmetric non-linear flow, in particular the short-time behavior due to internal resonances and the long-time behavior reflecting eigenvalues and eigenfunctions of the Hagen problem [20]. We performed similar tests for the long-time behavior of non-axisymmetric disturbances in the laminar runs. In the turbulent runs, we examined if our numerical results were compatible with the selection rules (17). E.g., when only the amplitudes belonging to $m = 1$, $l = 2$ and $m = -1$, $l = -1$ were different from zero in the beginning, then at first only the amplitudes belonging to $m = 0$, $l = 1$ would come up, and it would take much more time until other amplitudes grew.

The eigenvalues and eigenvectors (item v) were checked by reinsertion and graphical inspection; *the convergence was considered.* This is here of outmost importance since insufficient convergence may even pretend linear instability [21]. *For the approach via the vorticity equation* (4) *we found that the inclusion of Stokes modes with radial node indices n from* 1 *to* 15 *excludes this blunder if* $\mathrm{Re} \leq 3000$ *and* $|\beta| \leq 1$.

The results of the optimization (item vi) were examined by random trials.

Finally, the determinants (item vii) were checked by recomputing them as products of the eigenvalues of the matrices, and the eigenvalues were found by the QR algorithm. The relative difference between the determinants obtained from the two methods was never larger than 10^{-3}.

After all these checks we are convinced that we have no significant error in our numerical results. The only point subject to criticism is the truncation of the sum (7), i.e. that one should take more than N Stokes modes to approximate the true flow field.

3. Simulation

We report here the following results:

α) Our theory reproduces qualitatively or even semi-quantitatively several experimentally established facts, viz. the stability characteristics of pipe flow, the pressure drop caused by turbulence, the flattening of the velocity profile and the weird profile of velocity fluctuations. Nonagreements have all the same reason: Our solutions exhibit larger fluctuations than nature.

β) We also predict effects for which at most indications from measurements exist, namely a backflow close to one wall of the pipe correlated with an acceleration at the opposite wall, and a pressure which is essentially not constant over the pipe's cross section.

γ) It is established that turbulence gets its energy by a linear mechanism, despite of the linear stability.

δ) Some observations regarding the internal mechanics of turbulence will be communicated. The successful analysis of these observations (presented in the next chapter) constitutes evidence for the fundamental validity of our approach and indicates a possibility to manipulate turbulence.

'Mothers' and 'daughters' will be mentioned already in this chapter although these terms will be only defined in the next one. We do so to facilitate reference.

3.1 Transition to Turbulence

The Galerkin equations (13) and the formal apparatus developped in the previous chapter are general enough to comply with different physical situations. In this chapter we will discuss simulations performed with the following specifications: As contributions to the expansion (7) of the total velocity field the Stokes modes specified in Table 1 were selected.

I.e. for each block of given multipolarity m and axial node index l we included the Stokes functions with radial node indices n from 1 to 20. Hence 240 complex amplitudes $a_\mu(t)$ were in the play. Because of the reality conditions (33) this is equivalent to 240 degrees of freedom. $m = \pm 1$ means that only the simplest deviations from axial symmetry were taken into account. $l = \pm 1, \pm 2$ amounts to $\beta = \pm 0.5, \pm 1$ as allowed axial wave numbers since we take $L = 4\pi$ as periodicity length (cf. (10)). The important thing with all these Stokes modes is that none of them contributes to the total flux through the pipe. Only the Hagen-Poiseuille term in (7) has non-zero flux, and the

Table 1. Stokes modes for the constant-flux runs.

	$l=-2$	$l=-1$	$l=+1$	$l=+2$
$m=-1$	20	20	20	20
$m=0$	20	20	20	20
$m=+1$	20	20	20	20

Hagen-Poiseuille flow is, according to (8), presumed to be fixed. This set of Stokes functions describes therefore a pipe fed by pumps without feedback from the fluctuations of pressure; also no vessel to damp the pressure peaks should be used.

As evident from Table 1, we did not include $\beta = 0$ modes, i.e. no mean flow correction was taken into account. We did so because we wanted the set of modes as small as possible and thought it more important to permit at least in the crudest way formation of wave packets.

For the modes from Table 1, the Galerkin equations were solved as explained in Section 2.4. We studied systematically the behavior of the solutions with the following initial conditions:

$$\begin{aligned} \Re a_{1,-1,-2}(0) &= \Re a_{2,-1,-1}(0) = -A_0, \\ \Re a_{2,0,-2}(0) &= \Re a_{1,0,-1}(0) = A_0, \end{aligned} \tag{36}$$

or

$$\Re a_{1,-1,-2}(0) = \Re a_{2,-1,-1}(0) = -A_0 \tag{37}$$

or

$$\Re a_{1,-1,-2}(0) = \Re a_{1,-1,-1}(0) = -A_0 \tag{38}$$

or

$$\begin{aligned} a_{1,-1,-2}(0) &= a_{1,-1,-1}(0) = (1+i)A_0, \\ a_{1,0,-2}(0) &= a_{1,0,-1}(0) = (1+i)A_0, \\ a_{1,1,-2}(0) &= a_{1,1,-1}(0) = (1+i)A_0, \end{aligned} \tag{39}$$

where e.g. $a_{1,1,-2}(0)$ is shorthand for $a_{n=1,m=1,l=-2}$ $(t=0)$. A_0 denotes a parameter to vary the strength of the disturbance. In addition to the explicitly given initial conditions (36)–(39), the conditions of reality (33) had to be observed. All remaining amplitudes were set to zero.

A simple quantity to study the onset of turbulence is the energy of the disturbance $E_{\mathrm{dis}}(t)$ as introduced in (24). If $E_{\mathrm{dis}}(t) \to 0$ before $t = 500$, we say that we had a 'laminar run' although the beginning of such a run may look quite irregular (cf. Figure 6). If the irregular behavior persisted for times $t > 500$ we speak of a 'turbulent run' (cf. Figure 9). Runs with a long turbulent beginning ($t > 300$) but final return to laminarity were called 'laminar runs with a long turbulent transient'. We distinguished these runs because we think that it is difficult to discriminate them from intermittency. Figure 2 displays our results for the initial conditions (36) and (39). The following features are remarkable:

i) The 'double threshold' is obtained in either case, i.e. for Reynolds numbers smaller than a certain critical value $\mathrm{Re}_{\mathrm{cr}}$ no permanent turbulance arises, even for very strong initial disturbances. But it is not sufficient to cross the threshold marked by $\mathrm{Re}_{\mathrm{cr}}$. Moreover, the initial disturbance $E_{\mathrm{dis}}(t=0)$ has to be strong enough. It is thus possible to keep laminar flow in a pipe stable for arbitrary Reynolds numbers if accidental disturbances stay small enough. This second threshold is a decreasing function of the Reynolds number.

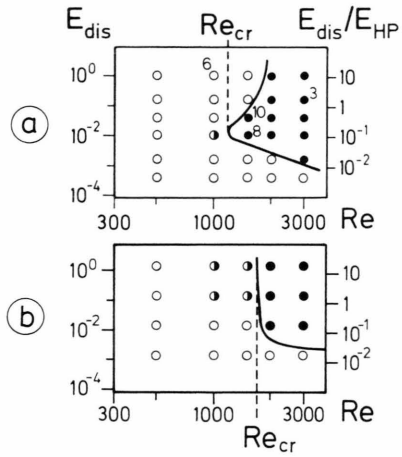

Fig. 2. The double threshold. The decision on laminarity (open symbols) or turbulence (filled symbols) in the plane spanned by the axes Reynolds number Re and energy of the disturbance E_{dis} at the start $t = 0$. Part a was calculated with the initial conditions (36), Part b with conditions (39). The numbers 3, 6, 8, 10 close to the symbols refer to Figs. 3, 6, 8, 10, respectively.

ii) The borderline between laminarity and turbulence depends on the initial conditions. If we assume that in experiments all sorts of disturbances are randomly produced, the best theoretical display for comparison would be obtained from an envelope of all possible borderlines, or in other words, one should take the borderline that extends as far leftward and downward as possible. Of all the initial conditions studied, the case (36) was most successful in this sense, closely followed by the case (37). This is because these initial conditions contain a mother ($a_{2,-1,-1}(0) \neq 0$) whereas all the others consist only of daughters ($a_{1,m,l}(0) \neq 0$) as will be explained in Section 4.1. A clear description of the double threshold from the experimentalist's point of view was given by Leite [22]. The experimental value for the critical Reynolds number is $\mathrm{Re}_{\mathrm{cr}} \approx 2000$ [23] whereas we find $\mathrm{Re}_{\mathrm{cr}} = 1500 \pm 500$ (see Figure 2). Leite presented also graphs of disturbances that decay though $\mathrm{Re} > \mathrm{Re}_{\mathrm{cr}}$; this data

(given in the Figs. 6 and 7 of [22]) is compatible with the borderlines in our Figure 2.

3.2 Statistical Properties of Velocity and Pressure

We calculated time averages of pressure differences

$$\overline{\Delta p}(r,\varphi) := \frac{1}{T}\int_0^T \Delta p(r,\varphi,t)\,\mathrm{d}t \tag{40}$$

and of velocities

$$\bar{u}_z(r,\varphi) := \frac{1}{T}\int_0^T u_z(r,\varphi,z=0,t)\,\mathrm{d}t \tag{41}$$

from the known solutions $a_\mu(t)$ of the Galerkin equations (13). For the evaluation, (31) and (7) with (A.4) were used. We computed the variances $\sigma_p^2(r,\varphi) := \overline{\Delta p^2} - \overline{\Delta p}^2$ and $\sigma_U^2(r,\varphi) := \overline{u_z^2} - \bar{u}_z^2$ in a similar way. Typical results are shown in Figs. 3 and 4. The main difference between these pictures is the averaging time T: In Fig. 3 it is $T = 400$ but $T = 1000$ for the data in Figure 4.

Consider first $\bar{U}(r)$ in Figure 3. $\bar{U}(r)$ is the total velocity in the direction of the pipe's axis with the customary contribution from the Hagen-Poiseuille flow, (8), plus the $\bar{u}_z$ from (41). The surprise with $\bar{U}(r)$ is that it takes negative values at $r \approx 0.9$. This indicates long-living back-flow close to the pipe's wall. Earlier in the run, no appreciable backflow could be seen, and still earlier it occurred on the other side of the pipe. In long-time averages, these fluctuations cancel. One obtains a velocity profile which is radially symmetrical, as observed in experiments. This is shown in Figure 4. Moreover, we find here a profile $\bar{U}(r)$ that is flattened as compared to the Hagen-Poiseuille profile $U_{\mathrm{HP}}(r)$. Unfortunately, no experimental data seems to be available for the transition to turbulence, viz. for $2000 < \mathrm{Re} < 3000$. Hence we had to insert measured values for $\mathrm{Re} = 4740$. For such large Reynolds numbers we could not do calculations because our low spatial resolution (cf. Table 1) was chosen for the study of the *onset* of turbulence.

The backflow has the following meaning: In the expansion (7) just two terms give the mayor contributions:

$$\boldsymbol{U}(r,t) \approx \boldsymbol{U}_{\mathrm{HP}}(r) + a_{1,\pm 1,l}(t)\,\boldsymbol{s}_{1,\pm 1,l}(r), \tag{42}$$

i.e. in addition to the Hagen-Poiseuille flow we see mostly a mode without nodes in radial direction, with multipolarity $m = +1$ or $m = -1$, and with some axial node index l. Such a flow is displayed in Figure 18. From this it follows that a backflow on one side of the pipe has to be compensated by a acceleration on the other side, as shown in Figure 3. Dinkelacker [24] claims that he observed such a correlation. This would prove the importance of the modes with $m \pm 1$ for the

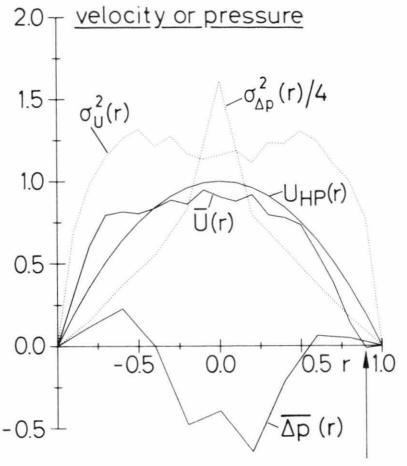

Fig. 3. Time-averaged velocity and pressure as functions of the distance r from the pipe's center line. Positive r means $\varphi = 0$ in (31), negative r corresponds to $\varphi = \pi$. Mean values are indicated by drawn lines, variances by dotted curves. The Hagen-Poiseuille profile is inserted for comparison. The arrow points to the region of largest backflow. The averages were calculated for a run with $\mathrm{Re} = 3000$ and $600 \le t \le 1000$. This run is marked in Fig. 2a by the 3.

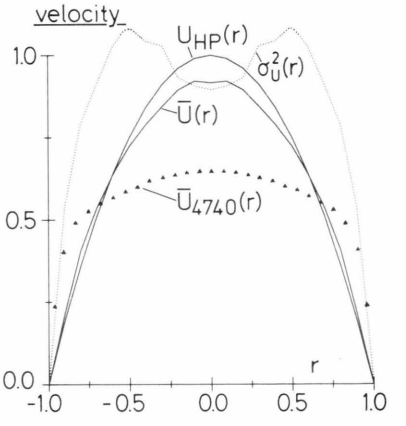

Fig. 4. Time-averaged velocity as function of the distance r from the pipe's center line. The marking is similar to that of Fig. 3, and it is even the same run, but averages were taken for $0 < t < 1000$. The data were furthermore symmetrized with respect to r and $-r$ to improve the statistics for further calculations, however, without essential effect on the view of the functions. Note that theoretical results for $\mathrm{Re} = 3000$ are compared with experimental ones at $\mathrm{Re} = 4740$ [23].

dynamics of turbulence. Similar conclusions can be drawn from photographs of the onset of turbulence, where colored streak lines looks like illustrations of (42). See, for example, the second picture on p. 61 of van Dyke's book [5]. One must not say that the other contributions to the expansion (7) are less important for the dynamics of the flow than those modes that were distinguished in (42). But the modes with $n=1$, $m=\pm 1$ determine the appearance of the transition. They are, in our terminology, the most striking daughters (cf. Sects. 4.1 and 4.3).

Calculated fluctuations $\sigma_U^2(r)$ of the velocity are also displayed in Figs. 3 and 4. These fluctuations are biggest somewhere between the pipe's wall and its center. Experimentally, this is a well-known effect [26, 27, 23]. Often the maximum of fluctuations is imagined to be closer to the walls ($r=\pm 1$), but this is true only for much bigger Reynolds numbers [26]. The data in Fig. 17 of Wygnanski's and Champagne's work [23] show, however, that our profiles of velocity fluctuations have the correct shape. But the absolute values are an order of magnitude larger in our computations than in the measurements.

The origin for this profile of the velocity fluctuations is found again in the $n=1$, $m=\pm 1$ modes. These modes have biggest velocities somewhere between the center and the wall of the pipe (cf. Figure 18).

Figure 3 displays furthermore the mean pressure $\overline{\Delta p}(r)$. It is predominantly negative indicating a pressure drop with the onset of turbulence. This is the most familiar effect of pipe turbulence. When one compares the values of our $\overline{\Delta p}(r=0)$ with experimental values, one finds the computed values more than an order of magnitude too large. There are, however, difficulties of interpretation which were addressed already in Section 2.3. These difficulties are obvious here since our $\overline{\Delta p}(r)$ depends essentially on r whereas the measured values were taken under the assumption that the pressure gradient does not. To get at least an estimate, we proceeded as follows: We defined a twice averaged pressure difference per length unit as

$$\widehat{\Delta p} := \frac{1}{\pi}\int_0^{2\pi}\int_0^1 \overline{\Delta p}(r,\varphi)\, r\, \mathrm{d}r\, \mathrm{d}\varphi \tag{43}$$

and computed the 'coefficient of resistance' by

$$\lambda := -16(\widehat{\Delta p} - 4/\mathrm{Re}). \tag{44}$$

$-4/\mathrm{Re}$ is the pressure gradient from Hagen-Poiseuille flow. Due to the integration in (43), the double average $\widehat{\Delta p}$ is much smaller than $\overline{\Delta p}(r=0)$. Restricted by insufficient statistics in most runs, we dared only in two cases to do the evaluation. The so obtained values are entered into Fig. 5 as open circles. The error of this data may be large. The fact that $\overline{\Delta p}(r,\varphi)$ is zero on the walls of the pipe follows from the definition (30) of that quantity. A proper pressure takes a fixed lower limit in the integral (3) and contributions from the linear part of the integrand. We suggest nevertheless that long-range pressure gradients are coped with by $\overline{\Delta p}(r,\varphi)$ because all other contributions to the pressure drop are spatially periodic.

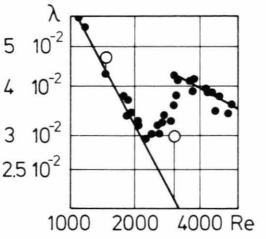

Fig. 5. The jump of resistance at the onset of turbulence. The coefficient λ is defined by (44) or, equivalently, in Schlichting's book [12, p. 611] where also the experimental data are taken from. The steep straight line on the left gives the coefficient of resistance for Hagen-Poiseuille flow valid for $\mathrm{Re}\to 0$; the line on the right is the asymptotic law for $\mathrm{Re}\to\infty$. The theoretical results are represented by the open symbols. The verticals connecting them to the Hagen-Poiseuille line exhibit the contribution (43) from the turbulent disturbance.

The last piece of information shown in Fig. 3 is the fluctuation of pressure $\sigma_P^2(r)$. It should be clear from the discussion in Sect. 2.3 that the peak of these fluctuations at the pipe's center must occur if the modes with $m=\pm 1$ play a significant part in pipe turbulence. No experimental data seems to be available for comparison with this theoretical finding.

3.3 Different Sorts of Energy Input

To get a first survey on the mechanics of pipe turbulence, we plotted in Figs. 6 through 9 six different quantities as functions of time t. The most important is E_{dis} (cf. (24)) which we take as indication for turbulence. Fig. 6, for example, displays the characteristics of a laminar run. The reason for return to laminarity is a too small Reynolds number; the initial strength of the disturbance $E_{\mathrm{dis}}(t=0)$ is huge. In contrast, for the run of Fig. 7, the Reynolds number was large enough for turbulence, but the initial strength of the disturbance was not sufficiently big. Figs. 8 and 9 show the typical features of turbulent runs. Exactly this discrim-

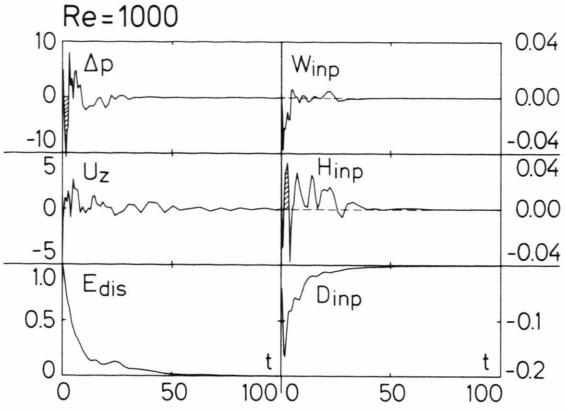

Fig. 6. Laminarisation because of a too small Reynolds number. Six global characteristics are displayed as functions of time t. Δp is shorthand for $\Delta p(r=0,t)$ (cf. (35)), and u_z substitutes $u_z(r=0,\varphi,z=0,t)$. The setup is explained in the text. The data are from the run marked in Fig. 2 by the 6. It was started on the initial condition (36) with $A_0 = 0.5$.

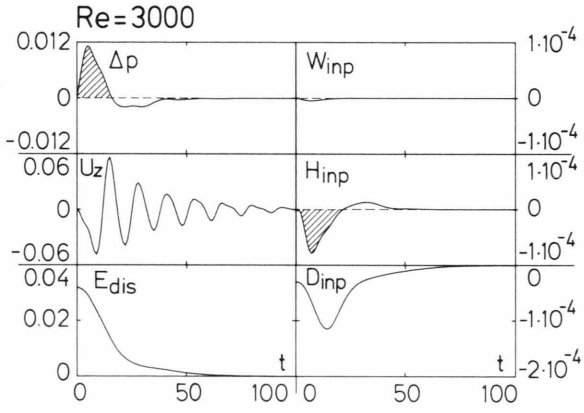

Fig. 7. Return to laminarity because of a too small initial disturbance. The display is similar to that of Figure 6. The run was started with the initial conditions (38) and $A_0 = 0.04$. Note the small numbers at the ordinates.

ination, namely the return of $E_{\text{dis}}(t)$ to zero as shown in Figs. 6 and 7 and, on the other hand, the never ending chaos as depicted in Figs. 8 and 9, was mapped into the open and closed dots of Figure 2.

It seems that the Galerkin equations (13) exhibit intermittency. In Fig. 8, we see a period of relative quiescence for $400 < t < 500$ which is typical for runs with Reynolds numbers close to the critical borderline (cf. Figure 2). In Fig. 9, the opposite phenomenon appears: Superimposed on average turbulence, powerful bursts occur at $t \approx 750$ and $t \approx 950$, as is typical in runs well above the critical Reynolds number. These

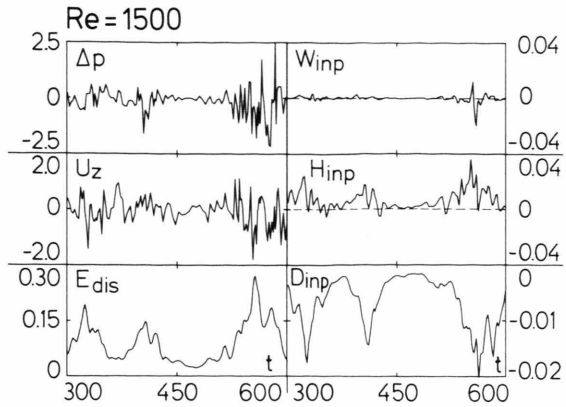

Fig. 8. Intermittency with quiescence. The data are from the run marked in Fig. 2 by the 8, i.e. initial conditions (36) with $A_0 = 0.05$.

two kinds of intermittency have counterparts in reality: The intermittency observed for transition to turbulence [12] looks different from the intermittency in fully developped turbulence [28].

The right-hand sides of the Figs. 6–9 display the different sorts of input defined in (25–27); their sum yields, according to (28), the increase of energy per unit time. The dissipation input D_{inp} stems from friction and is therefore always negative. The interaction input W_{inp}, which reflects the non-linearities, is mostly quite small and has long-time averages very close to zero. Hence there remains only one term to compensate the losses from friction. And indeed, Figs. 8 and 9 show an Hagen input H_{inp} which is almost always positive. This is amazing since instability in pipe flow cannot occur without non-linearities.

The energy supply is thus the business of the linear terms in the Galerkin equations (13). This conclusion will be supported in Sect. 5.1 where a related system of non-linear equations will be discussed. For that system, the interaction input even vanishes exactly, and yet the system goes to chaos.

The Figs. 6–9 show also the correspondence between the Hagen input and the velocity u_z on the pipe's axis. The latter was calculated from (7). Both quantities are linear functions of the amplitudes $a_\mu(t)$. It is therefore plausible that they have their strongest variations at the same times. In a comparison with experiments, our velocities seem to have, up to a factor, the correct dependence on time [29, 30].

But also the relation between the pressure differences Δp per length and the interaction input W_{inp}

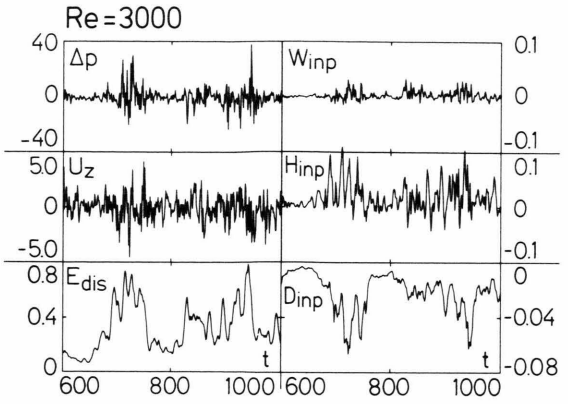

Fig. 9. Intermittency with bursts. The data are from the run marked in Fig. 2 by 3. A_0 was 0.2. Note the enormous values of Δp.

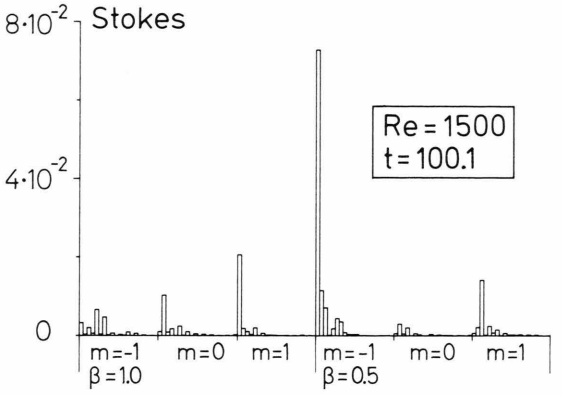

Fig. 10. Stokes spectra of nascent turbulence. The node index l is replaced by $\beta = 2\pi l/L$ to ease interpretation. The data are from the run indicated in Fig. 2 by the 10.

should be noted. Both are non-linear functions of the amplitudes $a_\mu(t)$. The interaction input assumes only sizable values if large-scale pressure differences take place. This was derived without approximations in Section 2.2 (see (21)). That the same correspondence is maintained by the approximate Galerkin equations (13), indicates once more the correctness of our calculations.

Finally we wish to draw attention to a phenomenon which might be useful in experiments. The run in Fig. 7 is a run with a 'bad start', i.e. even the sole support of turbulence, H_{inp}, draws energy from the disturbance, and this results in relaminarization of a relatively large disturbance. Such a rare event is correlated with an increase of pressure. The opposite can be observed in Figure 6: This run gets a much better start with a strong peak of H_{inp} shortly after the beginning. At the same time we see a drop of the pressure. In the Figs. 6 and 7 this correlation is set off by hatchings.

3.4 The Stokes Spectra

In the previous sections we have presented only global properties of the flow as a function of time or even averaged over time. We will give now a fairly complete account of the flow's state at some fixed time. To this end we prepared 'Stokes spectra'. These are histograms of $|a_{n,m,l}(t)|^2 =: 2E_{n,m,l}$ over the node indices n, m, and l. Due to the orthonormality relations (11) each of these terms has the meaning of an energy which is attributed to a specific Stokes mode. All together they give, according to (24), twice the total energy of the disturbance. The Figs. 10–12, which display some of these graphs, are organized as follows: We use the reality relations (33) to eliminate the modes with negative l. Hence only modes with positive wave number β appear. From the 240 remaining modes only 120 columns are formed because real and imaginary parts are combined in the moduli. The first 60 columns belong to modes with $\beta = 1.0$ or $l = 2$, the second 60 columns are for $\beta = 0.5$ or $l = 1$. Within these departments, there are blocks to discrimate modes with different multipolarities m. Each of these blocks contains 20 members corresponding to Stokes modes with ascending radial node index n. Hence the Stokes mode with the smallest damping is represented in every block by the column furthest on the left.

The common impression from all three Figs. 10–12 is that the $m = \pm 1$ modes carry more energy than the $m = 0$ modes. Another common phenomenon is the favor for odd n in the $m = \pm 1$ modes. These odd modes are essentially daughters (cf. Section 4.1). The figures demonstrate their overwhelming importance for the look of the disturbance. In the Figures 10 and 11 one of the $m = 1$, $n = 1$ modes is strongest. This is the agent responsible for the backflow shown in Figure 3. Figures 10 and 11 illustrate thus the meaning of (42).

Figure 10 stems from a turbulent run with a Reynolds number just above Re_{cr}. Such Stokes spectra we call spectra of 'nascent' turbulence: The contributions from $\beta = 0.5$ dominate, and a sharp spike for one of the $m = \pm 1$, $n = 1$ modes is observed. Figure 11, in

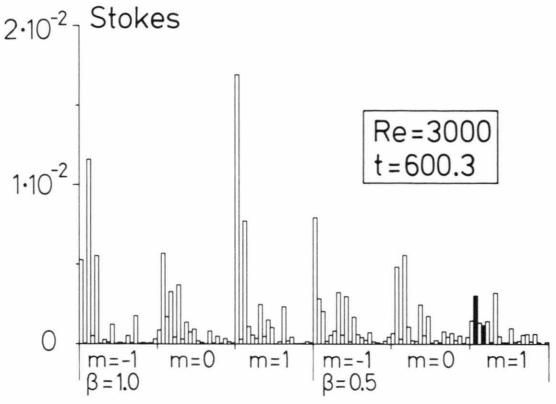

Fig. 11. Stokes spectra of 'developped' turbulence. The setup is as in Fig. 10. Data from the same run are displayed in Fig. 9, where also the violent products of the mother, shown here in black, can be seen.

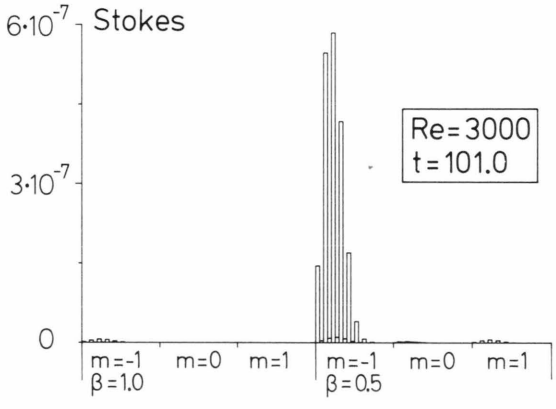

Fig. 12. Daughters close to laminarity. Note the small 'Stokes' energies $E_{n,m,1}$. This picture is from the end of the evolution displayed in Figure 7.

contrast, is to characterize 'developped' turbulence. The energy is more evenly distributed over the modes, and the department with $\beta = 1.0$ has now more strength. Moreover, here one is fortunate to watch a strong mother (cf. Sect. 4.1) distinguished by the black columns. This mother will still be modified until she fades and so gives rise to an outbreak of turbulence.

Figure 12, finally, exhibits the wretched remnants of turbulent beginnings. In all the blocks one just meets shrinking daughters. Most of them are already exceedingly small; only the structure for $m = -1$, $\beta = 0.5$ is still clearly recognizable.

Three problems are left for explanation: Why get the $m = \pm 1$ modes more power than their companions with $m = 0$? Why are the $m = \pm 1$ modes with odd n more intense than the even ones? And why is the turbulent energy shifted from the long-wave to the short-wave disturbances when the Reynolds number increases?

4. Mothers and Daughters

The weak point in our mathematical settings is the selection of Stokes modes as displayed in Table 1. One would like to include much more of them, in particular much more blocks with different multipolarities m and axial wave numbers β. In the next two chapters we will demonstrate that an extension cannot completely discard what we found. To show this, we proceed as follows:

α) We analyse the mechanism of the energy supply. Since this is a linear problem, it is orders of magnitudes easier than the non-linear one posed by eq. (2) and can therefore be solved with all desirable accuracy.

β) We relate the double threshold to the eigenvalues and eigenfunctions of the linearized problem and reveal the geometrical property of the eigenfunctions which causes the qualitatively different behavior of the $m = 0$ and $m = \pm 1$ modes.

The linear interactions are therefore sure to have been correctly taken into account. Inclusion of blocks in addition to those enumerated in Table 1 improves only the non-linear interactions. However, in the next chapter we will show that the essentials of turbulence do not depend on details of the non-linear terms.

The generally valid definition of 'mothers' and 'daughters' can be found at the end of Section 4.2.

4.1 The Quest of the Ideal Mother

The equation of motion which is linearized in the vicinity of the Hagen-Poiseuille flow $\boldsymbol{U}_{\mathrm{HP}}(r)$ follows from (4) as

$$\partial_t \boldsymbol{w} = \boldsymbol{V} \times (\boldsymbol{U}_{\mathrm{HP}} \times \boldsymbol{w} + \boldsymbol{u} \times \boldsymbol{W}_{\mathrm{HP}}) - 1/\mathrm{Re}\, \boldsymbol{V} \times \boldsymbol{V} \times \boldsymbol{w}. \tag{45}$$

$\boldsymbol{u}(\boldsymbol{r}, t)$ is the disturbance introduced in (1), and the vorticities are denoted by respective $\boldsymbol{W}$'s or $\boldsymbol{w}$'s. For the linear problem (45) the solutions were sought as an expansion

$$\boldsymbol{u}(\boldsymbol{r}, t) = \sum_{n=1}^{\infty} a_n(t)\, \boldsymbol{s}_{n,m,\beta}(\boldsymbol{r}). \tag{46}$$

The Stokes functions $s_{n,m,\beta}(r)$ are the same as in Section 2.1, but note that the sum in (46) is just a simple one, in contrast to the triple sum of (7); m and β are here fixed parameters. The usual Galerkin reduction leads again to equations of the type (13), but the interaction matrix does not occur. Since the remaining matrices H and D are both diagonal with respect to m and β (see (18)), much smaller systems of ordinary differential equations can be worked with. Using only the modes with $n = 1, 2, \ldots, 20$ gives already accurate results. We know this since checks with $n = 1, \ldots, 30$ or even with $n = 1, \ldots, 50$ were done throughout.

First we solved (45) with the initial condition

$$u(r, t = 0) = s_{n_0, m, \beta}(r) \tag{47}$$

for various values of m, β, and n_0. For $m = 0$ we obtained only decreasing disturbances, as expected from the linear stability of pipe flow. For $m = 1$ the results depended on n_0: For odd n_0, decreasing disturbances were observed; for even n_0, we found strongly increasing amplitudes. There is no contradiction to linear stability since linear stability is an asymptotic property for long times, whereas our disturbances increased only for a limited time. From these observations we derived a working definition:

The Stokes modes with $m = \pm 1$ and even radial node indices n are called mothers. The stokes modes with $m = \pm 1$ and odd radial node indices n are called daughters.

The value of β is unimportant as long as $0 < \beta < 2$. The word 'mother' was chosen since these initial conditions obviously produce something, and it soon turned out that the products are indeed 'daughters' (cf. Fig. 27 below). The working definition was nevertheless dissatisfactory because it refers to the Stokes functions; we deal, however, with a partial differential equation (45) for which the Stokes functions are nothing but a tool.

Therefore we looked for an amplified disturbance which should be a sole property of (45). This disturbance was afterwards named the 'ideal mother'. It is defined by the following prescription;

The initial conditions must be varied until the largest possible energy $E_{\mathrm{dis}}(t = t_{\max})$ is obtained. In doing so, the initial energy has to be kept fixed.

$E_{\mathrm{dis}}(t = t_{\max})/E_{\mathrm{dis}}(t = 0)$ is thus for fixed β the maximum amplification of energy. The realization of the prescription was straightforward: Some initial condition was chosen, and (45) was integrated until the disturbance reached its maximum. The so obtained $E_{\mathrm{dis}}(t = t_{\max})$ was stored, and the process was repeated with another initial condition. To satisfy the constraint, the amplitudes $a_n(0)$ were represented by multi-dimensional spherical coordinates:

$$\begin{aligned}
&\Re a_2(0) = f_1 \cos\theta_1, && \Im a_2 = 0,\\
&\Re a_4(0) = f_2 \cos\theta_2, && \Im a_4 = f_3 \cos\theta_3,\\
&\ldots && \ldots\\
&\Re a_N(0) = f_{N-2} \cos\theta_{N-2}, && \Im a_N(0) = f_{N-1} \cos\theta_{N-1},\\
&\Re a_1(0) = f_N \cos\theta_N, && \Im a_1(0) = f_{N+1} \cos\theta_{N+1},\\
&\ldots && \ldots\\
&\Re a_{N-1}(0) = f_{N-2} \cos\theta_{2N-2}, && \Im a_{N-1}(0) = f_{2N-1}
\end{aligned} \tag{48}$$

with

$$f_1 := 1, \quad f_{n+1} := f_n \sin\theta_n \quad \text{for} \quad n = 1, 2, 3, \ldots, 2N - 2.$$

N must be an even number. We had mostly $N = 12$ and therefore 22 degrees of freedom for the optimization. In (48) the amplitudes with even radial node indices are the first in the list. This is numerically advantageous because of the minor importance of the odd Stokes modes for the structure of the ideal mother. The computational procedure is referenced in Section 2.4.

Table 2 presents the outcome of an optimization. The corresponding Stokes spectrum is shown in Fig. 26 below. It is seen that a mother in general contains also odd Stokes contributions. The working definition therefore is only approximately valid.

One can do these optimizations for many values of β and Re. We collected our achievements in Figure 13. It displays the maximum amplification and $t_{\max}$, viz. the time at which the disturbance has reached its maximum. The 'return time' is also shown in Fig. 13. It is

Table 2. Angles θ_n of an ideal mother at $m = 1$, $\beta = 1.0$, and Re = 2000.

$n =$	1	2	3	4	5	6	7	8	9	10	11
$\theta_n =$	83°	94°	−67°	56°	−84°	−74°	57°	104°	117°	71°	87°
$n =$	12	13	14	15	16	17	18	19	20	21	22
$\theta_n =$	86°	87°	103°	−79°	69°	64°	132°	69°	85°	149°	53°

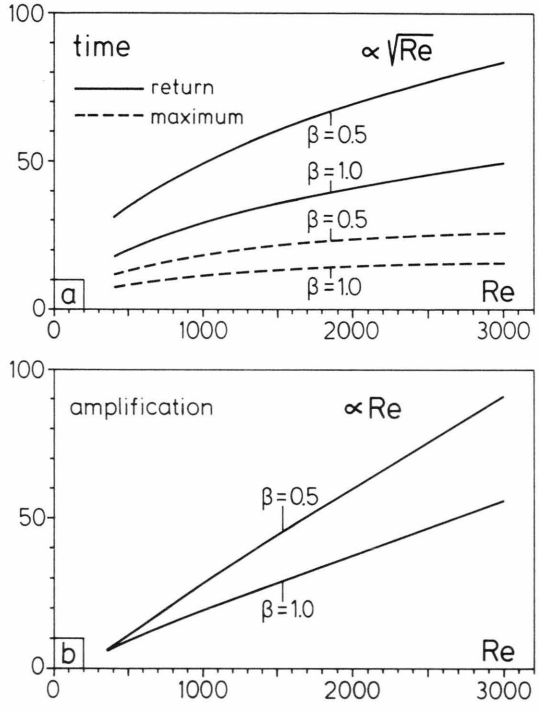

Fig. 13. Return and maximum times (Part a) as well as energy amplification (Part b) by ideal mothers. All calculations were done for $m = 1$, one part for $\beta = 0.5$, the other for $\beta = 1.0$. The symbols $\propto \sqrt{\mathrm{Re}}$ and $\propto \mathrm{Re}$ indicate the approximate dependence on the Reynolds number Re of the functions in the concerning parts.

defined as the time $t_{\mathrm{ret}} > t_{\max}$ for which the disturbance has returned to its initial strength, $E_{\mathrm{dis}}(t_{\mathrm{ret}}) = E_{\mathrm{dis}}(0)$. The meaning of these definitions should be obvious from the graphs in Figure 1: The sum of the two energies considered there, $E_{\mathrm{M}} + E_{\mathrm{T}}$, corresponds to the energy E_{dis} used here.

The message of Fig. 13 is that transient amplification of an initial disturbance by a factor of 100 is possible and that these transients live for a long time. The linearity of the energy supply, stated in Sect. 3.3, is thus confirmed. But this raises further questions: Can one understand amplification in a linearly stable system by a simple model? Which counterpart has the effect in the properties of the eigenvalues and eigenfunctions? And how is a transient amplification turned in permanent chaos? These questions will be answered in the next sections.

4.2 The Mother-Daughter Mechanism as a Textbook Problem

We derive here the effects of Sect. 4.1 found by numerical calculation from a simple, analytically solvable model. Its equation of motion will be

$$d_t \boldsymbol{a}(t) = (H + D)\,\boldsymbol{a}(t). \tag{49}$$

The disturbance has only two components: $\boldsymbol{a}(t) = (a_1(t), a_2(t))$, and as substitutes for the Hagen and dissipation matrices (factor 1/Re incorporated) we take

$$H := i\begin{pmatrix} h & g \\ 0 & h \end{pmatrix}, \quad D := \begin{pmatrix} -d+\delta & 0 \\ 0 & -d \end{pmatrix}. \tag{50}$$

The parameters h, g, d, and δ are all assumed to be real numbers. d must be furthermore positive and δ smaller than d. By this we map the most important properties of the prototypes defined in (15) and (16). The zero in the Hagen matrix means no loss of generality since it can always be generated by an orthogonal transform. It is, however, restrictive that both diagonal elements in H are assumed to be equal, but this simplification is essential as we look for a special effect. For the same reason we assume that δ is much smaller than d. The general solution of (49) can at once be written as

$$\boldsymbol{a}(t) = \alpha_1 \begin{pmatrix} 1 \\ 0 \end{pmatrix} e^{(ih-d+\delta)t} + \alpha_2 \begin{pmatrix} 1 \\ i\delta/g \end{pmatrix} e^{(ih-d)t}. \tag{51}$$

The complex constants α_1 and α_2 have to be determined from the initial conditions. The vectors in front of the exponentials are the eigenvectors of the eigenvalue problem of (49); the eigenvalues are met in the exponentials between the brackets. For $\delta \to 0$ the eigenvectors become parallel. They point then both into the a_1-direction.

Further we introduced the at first sight arbitrary naming

$$\text{daughter:} \begin{pmatrix} 1 \\ 0 \end{pmatrix}, \qquad \text{mother:} \begin{pmatrix} 0 \\ 1 \end{pmatrix} \tag{52}$$

and took first the daughter as initial condition. From (51) there follows

$$\boldsymbol{a}(t) = \begin{pmatrix} 1 \\ 0 \end{pmatrix} e^{(ih - d + \delta)t} \tag{53}$$

with the energy

$$E_T(t) = \tfrac{1}{2}\, e^{-2dt}, \tag{54}$$

which is because of $d > 0$ a monotonously decreasing function. In the exponent of (54), an insignificant term with δ was neglected. In the second case, the mother furnished the initial condition. From (51) we got

$$\boldsymbol{a}(t) = \frac{ig}{\delta} \left\{ \begin{pmatrix} 1 \\ 0 \end{pmatrix} e^{(ih - d + \delta)t} - \begin{pmatrix} 1 \\ i\delta/g \end{pmatrix} e^{(ih - d)t} \right\} \tag{55}$$

and reordered this to obtain

$$\boldsymbol{a}(t) = \begin{pmatrix} ig/\delta \\ 0 \end{pmatrix} (e^{\delta t} - 1)\, e^{(ih - d)t} + \begin{pmatrix} 0 \\ 1 \end{pmatrix} e^{(ih - d)t}. \tag{55'}$$

Despite of its triviality the last transformation is of outmost importance for the understanding of the mother-daughter effect: One sees that the mother has to be represented by a difference of eigenvectors with overflowing cancellations if δ goes to zero; and the reordering exhibits a generally large term. For $\delta \to 0$, (55') can be further simplified:

$$\boldsymbol{a}(t) = \begin{pmatrix} ig \\ 0 \end{pmatrix} t\, e^{(ih - d)t} + \begin{pmatrix} 0 \\ 1 \end{pmatrix} e^{(ih - d)t}. \tag{56}$$

On comparing this with (52), one sees that the first term on the right-hand side is proportional to the daughter while the mother occurs in the second. The remarkable fact is the factor t at the daughter describing transient growth. And indeed, the energy of the disturbance is now

$$E_T + E_M = \tfrac{1}{2}\, g^2 t^2\, e^{-2dt} + \tfrac{1}{2}\, e^{-2dt}, \tag{57}$$

i.e. the daughter's contribution first increases quadratically with time, whereas the mother's part dies off at once. Graphs of the functions E_T and E_M are shown in Figure 1.

From these equations, we abstracted four characteristics of mothers and daughters:

C1: A motherless daughter fades (cf. (54)).
C2: A mother must produce a daughter ((55) and (55')).
C3: A daughter grows as long as her mother lives (56).
C4: A mothers's part in the evolution decreases always (57).

These considerations exhibit just some phenomenological similarities with the numerical findings from the previous section. But in the comparison one can go a step further: The disturbance of (57) gets its maximum energy at $t_{\max} = (2d)^{-1} + \sqrt{(2d)^{-2} - g^{-2}}$. For an order-of-magnitude estimate

$$t_{\max} \approx 1/d \tag{58}$$

is good enough because the inequality $|g| \gg d$ is always right for sufficiently large Reynolds numbers (see the description of Figure 15). With the same quality of accuracy one finds from (57) the maximum amplification as

$$E_{\text{dis}}(t_{\max}) \approx \frac{1}{2e^2} \left(\frac{g}{d}\right)^2. \tag{59}$$

Now, from the eigenvalue analysis of the proper pipe problem (see Fig. 15 below) we know that the parameter d varies as $\mathrm{Re}^{-1/2}$ while g remains essentially constant. This gives inserted into (58) and (59):

$$t_{\max} \propto \mathrm{Re}^{1/2}, \qquad E_{\text{dis}}(t_{\max})/E_{\text{dis}}(0) \propto \mathrm{Re}. \tag{60}$$

Exactly these trends are observed in Figure 13.

Every reader acquainted with linear algebra certainly has remarked that we have discussed only well-known properties of non-symmetric linear systems. For $\delta = 0$, the matrix $H + D$ is the Jordan matrix which has in two-dimensional space only one eigenvector, i.e. it is a simply *defective* matrix [31, 32, 16]. That the corresponding system of differential equations has components in its solutions which increase algebraically with time, is tought in undergraduate courses when the aperiodic limiting case of the damped harmonic oscillator is discussed. And the parameter δ was only introduced to stress that the effects do not disappear if the condition of defectiveness is not exactly fulfilled.

In practise, a linearized problem is scarcely ever exactly defective. To measure defectiveness, we calculate the volume of the parallelepiped spanned by the normalized eigenvectors; a system is the more defective the smaller this volume is as compared to unity. For our simple model the volume is

$$\mathrm{Vol} = \frac{1}{\sqrt{(g/\delta)^2 + 1}}, \tag{61}$$

which vanishes as δ goes to nil.

The fact that a dynamical system has a nearly defective linear part is nevertheless not trivial. First the linear operator must not be selfadjoint or, in other words, the Hagen matrix must not be symmetrical. For the present problem this is the case, as can be seen from (45) and (15). Second, several eigenvalues must be close to each other, and the related eigenvectors must be nearly collinear. That this is the case for pipe flow, will be demonstrated in the next two sections. Third, the deviations from asymmetry must be large enough to warrant sufficient amplification. In our simple model this is expressed by the condition $|g/d| \gg 1$ (cf. (59)). That it is true for pipe flow, was shown in the previous section (cf. Figure 13).

At last we are in the position to give the general definition of daughters and mothers:

In the time-dependent, linearized, and stable problem transient amplification must be possible. Daughters can be expanded in terms of the eigenfunctions, and the expansion coefficients stay all small. Mothers can only be reached with large coefficients or have no expansion at all.

In this definition it is presumed that all mothers, daughters, and eigenfunctions are normalized; 'large' means then much greater than unity. In the limit of totally defective systems the daughters lie in the space spanned by the eigenvectors, while only the higher principal vectors can form the mothers.

4.3 Hagen Functions and the Loss of Toroidality

We prove here that the ideas developped in the previous section apply to pipe flow. The objective is to understand the structure of the eigenvalue problem

$$\beta c \nabla \times \boldsymbol{h}_c = \nabla \times (\boldsymbol{U}_{\mathrm{HP}} \times \nabla \times \boldsymbol{h}_c + \boldsymbol{h}_c \times \boldsymbol{W}_{\mathrm{HP}}) - 1/\mathrm{Re}\, \nabla \times \nabla \times \nabla \times \boldsymbol{h}_c \tag{62}$$

which is derived from (45) by splitting the factor $e^{\beta c t}$ from the disturbance $\boldsymbol{u}(\boldsymbol{r}, t)$. The same boundary conditions as in (5) and (6) have to be applied. The reason for decomposing the eigenvalue as βc is that this gives the possibility to interprete $-c_i := -\Im c$ as a phase velocity. The eigenfunctions $\boldsymbol{h}_c(\boldsymbol{r})$ will be called 'Hagen functions'. As the time-dependent system (45), the eigenvalue problem (62) can be solved for each m and β separately. Hence we computed the Hagen functions by a series similar to (46),

$$\boldsymbol{h}_c(\boldsymbol{r}) = \sum_{n=1}^{\infty} a_n(c)\, \boldsymbol{s}_{n,m,\beta}(\boldsymbol{r}), \tag{63}$$

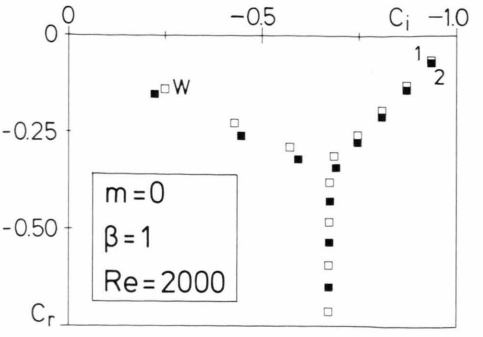

Fig. 14. Hagen eigenvalues in the plane of phase velocity c_i and logarithmic increment c_r for multipolarity $m = 0$. The eigenfunctions which belong to the eigenvalues marked by 1 and 2 are center modes shown in Figs. 20 and 21. The eigenfunction of w is the wall mode depicted in Figure 22. The eigenvalues indicated by the open squares were calculated only with odd Stokes functions, whereas the closed squares stem from the even Stokes functions. As a consequence, the eigenfunctions of even these close eigenvalues are orthogonal to each other as can be checked e.g. when Figs. 20 and 21 are compared. Therefore the neighborhood of eigenvalues has here nothing to do with defectiveness. For the computation of each of the two sets of eigenvalues, the sum (63) was normally truncated at $n = 41$.

and checked results with truncation at $n = 71$. The argument c in the expansion coefficients a_n is to remind that the set of these coefficients has to be computed for every eigenvalue anew.

The eigenvalues c are shown for two cases in the Figs. 14 and 15. Their structure may be visualized as a two- or three-finger swearhand with a piece of the arm below, fingers upmost right and left, and a palm in the center. Linear stability is expressed by the fact that none of the eigenvalues has a positive real part $c_r = \Re c$. The eigenvalues in the arms belong to functions which are essentially unmodified Stokes modes. These strongly damped modes swim with the Hagen-Poiseuille flow without sensing its profile. Thus they get all the same average velocity $-c_i \approx 2/3$. The eigenvalues in the fingers belong either to the 'wall' or to the 'center' modes. Center modes have velocities close to 1 i.e. they feel the central part of the Hagen-Poiseuille flow (see Figs. 20, 21, 23, and 24). The wall modes take their largest amplitudes close to the pipe's wall, and so they are slow (see Figs. 22 and 25).

Strongly damped, wall, and center modes are known [2]. We are going to show that they don't matter for the onset of turbulence, in contrast to what was believed hitherto [7]. Important for turbulence is the palm of the hand, in particular the set of eigenvalues in Fig. 15 which is encircled.

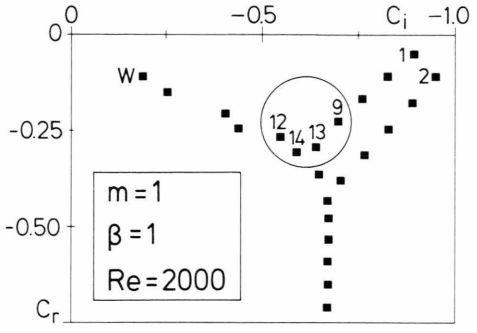

Fig. 15. Hagen eigenvalues in the plane of phase velocity c_i and logarithmic increment c_r for $m = 1$. The center functions of 1 and 2 are pictured in Figs. 23 and 24. The wall function of w appears in Figure 25. The circle encompasses the 'birthplace of turbulence'; the Hagen functions with the numbers 9, 12, 13, and 14 have superior importance as can be seen from the Hagen spectrum in Figure 26. For computation, the sum (63) included the terms $n = 1, 2, 3, \ldots, 50$. When pictures like this are made for various Reynolds numbers, one finds that the center of the circle moves mainly in the vertical direction. More precisely, if the coordinates of the circle's center are denoted by $d + ih$, one obtains $d \approx -10\,\mathrm{Re}^{-1/2}$, whereas $h \approx -0.6$ is essentially independent of the Reynolds number. d and h are numbers used in Section 4.2. Executing a somewhat more involved procedure shows that also the equivalent of g (Sect. 4.2) does not crucially depend on Re.

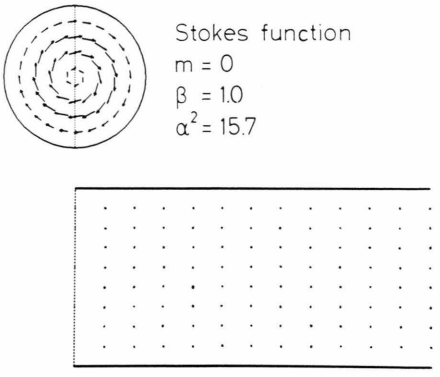

Fig. 16. Stokes function for $m = 0$ with lowest radial node index ($n = 1$). All Figures from 16 to 26 show a transverse and a longitudinal cut through the pipe so that both cuts join at the dotted lines. (The dots are in some of the figures perhaps not easily recognizable.) The characteristics of the vector functions are entered in the right upper corner of the figures. Here it is multipolarity m, wave number β, and eigenvalue α^2. The mathematical meaning of these symbols is defined in (9) and (10). The present Stokes function is the standard example for a toroidal mode. All odd $m = 0$ Stokes functions represent toroidal modes. The computation was performed using the formulas from the Appendix.

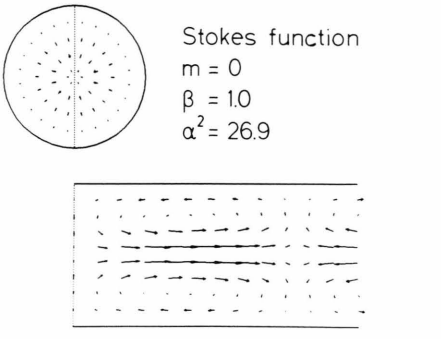

Fig. 17. Stokes function for $m = 0$ with radial node index $n = 2$. All even $m = 0$ Stokes functions represent meridional modes.

There is another discrimination between sets of eigenfunctions, which is indicated in Fig. 14 by open and closed squares. We distinguish here between 'toroidal' and 'meridional' modes. A typical toroidal Stokes function is shown in Fig. 16, a meridional one in Figure 17. The difference is that for the toroidal function the z-component of the velocity u_z is zero, whereas the φ-component u_φ reaches sizable values. For the meridional function, on the contrary, u_φ disappears while u_z is present.

In the case of axial symmetry ($m = 0$) meridionality and toroidality are cleanly separated. For the Stokes functions, this follows from the charateristic equation (A.7), which factorizes if $m = 0$. For the $m = 0$ Hagen functions, this follows from the characteristic equation tion is possible [2]. The underlying reason is that the pipe's symmetry group for axial symmetry is just the one-dimensional translation group. For the disturbances without axial symmetry, however, the group consists of translations along and rotations about the axis, and in the extended group neither Stokes nor Hagen functions can be expected to form reducible tensorial sets. For the Stokes functions this is visualized in the Figs. 18 and 19: The sharp difference between meridional and toroidal functions is gone. But one still may keep a modified criterion: A pipe function is called 'toroidal' if $|u_\varphi| > |u_z|$ or 'meridional' in the opposite case where the vertical bars indicate some suitable norm. In this sense one may say that the Stokes function in Fig. 18 is meridional, whereas that in Fig. 19 is toroidal.

If we look now on the Hagen functions with multipolarity $|m| = 1$ (Figs. 23–25), we see a dramatic difference: All the $m = 1$ functions lack toroidality. And this holds for the center functions (Figs. 23, 24) as well as for the wall functions (Figure 25). Systematic examination reveals that all functions belonging to the

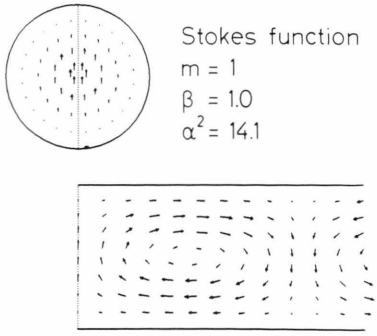

Fig. 18. Stokes function for $m = 1$ with lowest radial node index $n = 1$. This mode is the most important constituent of most daughters (cf. the Stokes spectrum in Fig. 27 at $t = 21.4$).

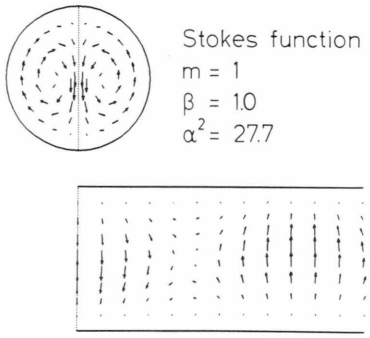

Fig. 19. Stokes function for $m = 1$ with radial node index $n = 2$. This mode is a mother, but by far not the best one (cf. Sect. 4.1).

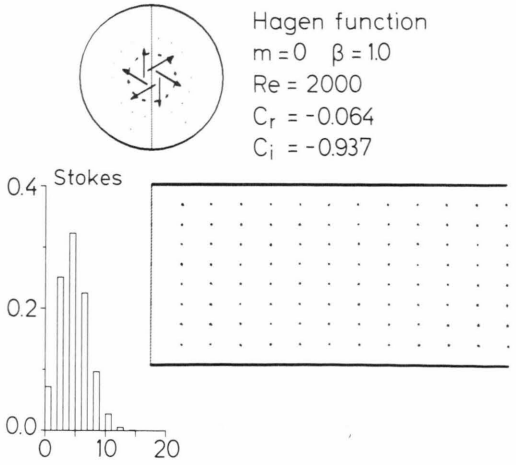

Fig. 20. Axially symmetric Hagen function with smallest damping. (See the value of c_r in the upper right panel.) The corresponding eigenvalue is marked in Fig. 14 by 1. The lower left part exhibits that only odd Stokes functions were necessary for the representation of this toroidal center function. See Fig. 16 for comparison.

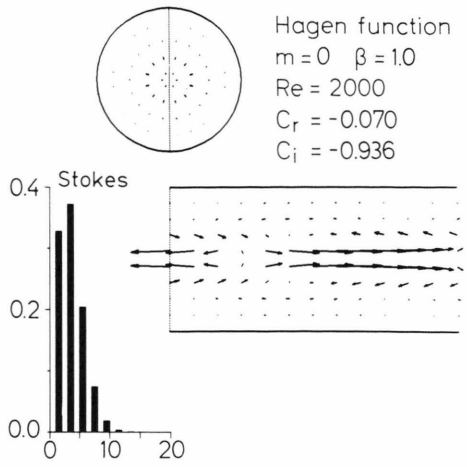

Fig. 21. Axially symmetric Hagen function which is related to the eigenvalue 2 in Figure 14. Geometric representation, velocity c_i, and Stokes spectrum reveal that this is a meridional center function. For example, the Stokes function shown in Fig. 17 is contained in this Hagen function. In this and the following figures, the even columns are painted black to stress the difference between odd and even Stokes contributions.

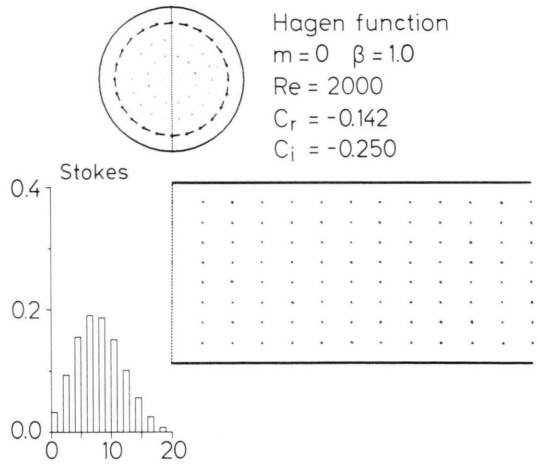

Fig. 22. Axially symmetric Hagen function related to the w in Figure 14. We have here the best example for a toroidal wall mode. Compare this again with Figure 16.

fingers and to the palm are crippled in this way and that things get better only for the strongly damped modes ($c_r < -0.5$). Physically the loss of toroidality happens since the disturbances swim with the purely meridional Hagen-Poiseuille flow, and correspondingly they are stretched. Toroidality can only survive when it is protected by the symmetry property mentioned above.

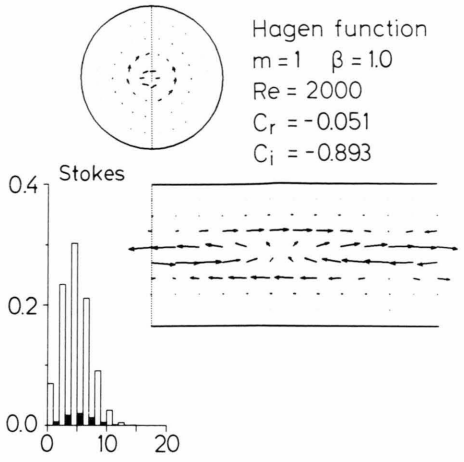

Fig. 23. Non-axisymmetric Hagen function belonging to the eigenvalue 1 in Figure 15. Note the smallness of the even contributions in the Stokes spectrum and the size of the velocity component u_z in the longitudinal cut.

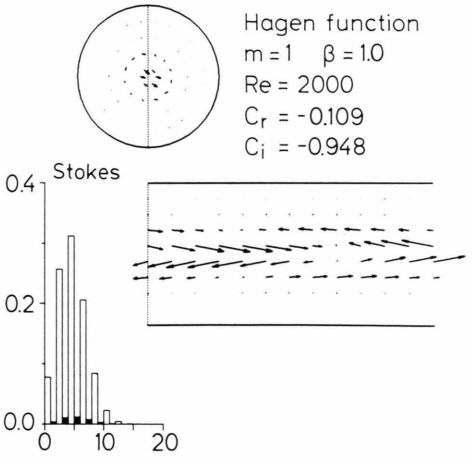

Fig. 24. Non-axisymmetric Hagen function of the eigenvalue 2 in Figure 15. The contributions from the even Stokes functions are small again.

The Stokes spectra displayed in the Figs. 20 through 25 contain a similar information. The axially symmetric Hagen functions (Figs. 20–22) have either odd or even Stokes components. But the $m = 1$ Hagen functions receive much more strength from odd Stokes functions than from the even ones.

All this establishes a complete analogy to the model of the previous section: The eigenvectors there, (51), were almost parallel; the Hagen functions here avoid all flow patterns with an appreciable toroidal component, and therefore toroidal functions can only be

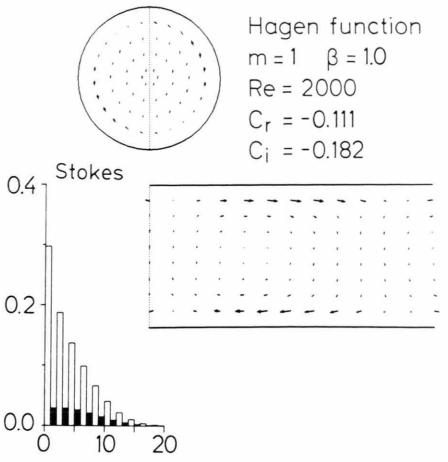

Fig. 25. Non-axisymmetric Hagen function for the eigenvalue w in Figure 15. Again this is mostly a combination of even Stokes functions. The closest Stokes analog is depicted in Figure 18.

expanded in the basis of Hagen functions if the coefficients are allowed to become very large. A striking example is the ideal mother from Table 2. The same mode is displayed in Figure 26. We see that it is a toroidal function, that it has large contributions from the even Stokes functions, and that the coefficients for expansion in the Hagen basis are gigantic. The last fact can be read from the 'Hagen spectrum', which is defined via

$$\boldsymbol{u}(\boldsymbol{r}) = \sum_{l=1}^{\infty} \gamma_l \boldsymbol{h}_{c_l}(\boldsymbol{r}) \tag{64}$$

as a histogram of the absolute squares $|\gamma_l|^2$ over the order index l of the eigenvalues.

The behavior of the time-dependent solutions described in Section 4.1 is now also understandable. Namely, the disturbance can be written as

$$\boldsymbol{u}(\boldsymbol{r}, t) = \sum_{l=1}^{\infty} \gamma_l e^{c_l t} \boldsymbol{h}_{c_l}(\boldsymbol{r}). \tag{65}$$

In the series everything is known as soon as the eigenvalue problem (62) is solved and the expansion (64) for the initial perturbance is performed. On the left-hand side of (65) we have a function of moderate size. On the right-hand side there is a sum with enormous terms. The contradiction can be resolved only if huge cancellations occur. We can even tell what exactly is cancelled: mostly the meridional parts of the Hagen functions to give their small toroidal parts a chance to show up. The cancellation, however, is only good at

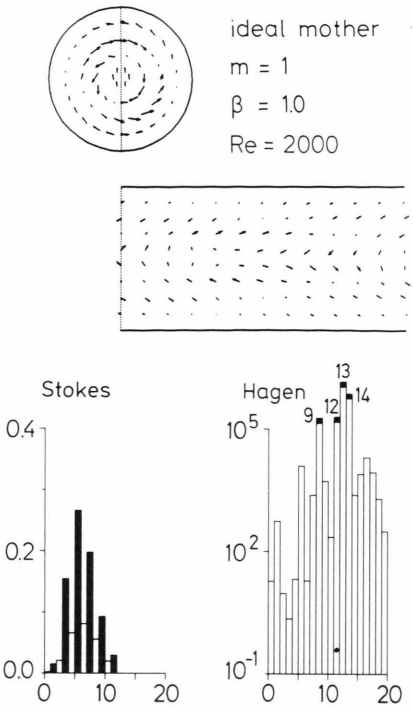

Fig. 26. An ideal mother. The most prominent contributions in the Hagen spectrum are highlighted by the black tips. The respective eigenvalues are those encircled in Figure 15. The same numbers occur in Table 3. Stokes and Hagen spectra are ordered so that the contributions from the modes with smallest damping appear on the left.

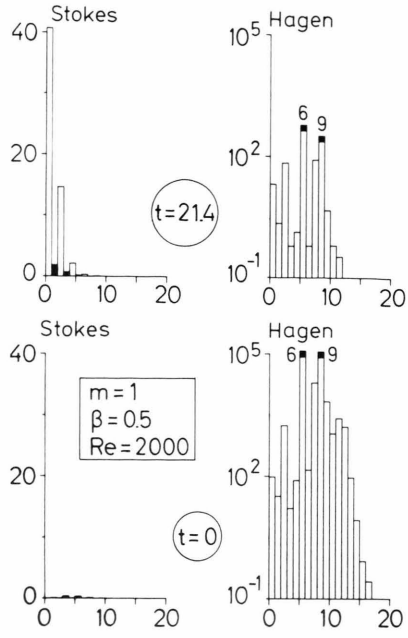

Fig. 27. Evolution of an ideal mother. At $t = 0$ the Stokes components are so small that is takes care to see them; they are predominantly even, as in the mother of Figure 26. (According to the working definition in Section 4.1, even Stokes modes are mothers.) The Hagen contributions, in contrast, are gigantic. But the two largest components 6 and 9 cancel almost perfectly. At $t = 21.4$, a Stokes spectrum which consists mainly of odd contributions has arisen. (Following the working definition this means that daughters were generated.) The 6 in the Hagen spectrum is not anymore compensated.

$t = 0$. For other times, the relative size of the factors $e^{c_l t}$ is different. Therefore, as time goes on, the destructive interference is abolished, at least one of the Hagen modes can appear without being extinguished by his brethren, and energy is released. The process is analyzed in Fig. 27; it is evidently the same as described on the transition from (55) to (55′). Furthermore, the characteristics C1 to C4, derived in Sect. 4.2 from the simple model, are now understood as being general properties of the mother-daughter process.

4.4 Collective Defectiveness

Why is the palm in Fig. 15 so important? First, of course, because the eigenvalues approach each other closest in the palm, and proximity of eigenvalues is a necessary condition for defectiveness. A sufficient criterion is obtained from the absolute square of the correlation function

$$C_{kl} := \int_{(\text{pipe})} \boldsymbol{h}^*_{c_k}(\boldsymbol{r})\, \boldsymbol{h}_{c_l}(\boldsymbol{r})\, \mathrm{d}\tau. \tag{66}$$

Table 3. Almost defective pairs of Hagen functions for $m = 1$, $\beta = 1.0$, and $\mathrm{Re} = 2000$. The expression C_{kl} is defined in (66). The Hagen functions are sorted according to damping.

k	8	9	12	13	13	14
l	10	13	14	14	16	16
$1 - \lvert C_{kl}\rvert^2$	0.11	0.15	0.08	0.06	0.09	0.13

If the expression $1 - |C_{kl}|^2$ is small compared to 1 for some pair of Hagen functions k and l, we know savely that the eigenvalue problem (62) is close to defectiveness. Table 3 gives an account of the Hagen functions with strongest correlations.

A comparison of this table with Fig. 15 shows that all the most collinear Hagen functions belong to the palm. Moreover, the most collinear functions need also the largest expansion coefficients for the representation of a mother. Fig. 26 is evidence for this.

But Table 3 introduces also a new point of view: It demonstrates that there are more than two eigen-

functions in approximate collinearity. Examination with other values of β and Re exhibits 'collective defectiveness' to be typical. A destructive interference with only two dominant terms as shown in Fig. 27 is a rare case; it was presented only to simplify visualization.

Knowledge concerning this point is important if the permanence of turbulence is to be understood. The mother-daughter effect is a linear mechanism. Without non-linearity it remains a transient phenomenon as the daughters die off when the mothers are gone. The non-linearity has to fill the gap by recreating mothers when the daughters are most abundant. But the non-linearity just mixes modes without knowing anything about mothers. One should therefore guess that the recreation can only work if almost every remixed flow is a mother. We shown now: For the multipolarity $m = 1$ almost all disturbances are mothers.

To this end the notion 'almost all' has to be given a precise meaning. Using the kinetic energy (20) to define a scalar product, it is standard business to establish a Hilbert space of disturbances in which the Stokes functions $\boldsymbol{s}_{n,m,\beta}(\boldsymbol{r})$, with m and β fixed, generate a suitable basis. We took the so introduced lengths and angles to measure volumes: As a reference we chose the set R of disturbances $\boldsymbol{u}(\boldsymbol{r})$

$$R: = \left\{ \boldsymbol{u}(\boldsymbol{r}) \,|\, \boldsymbol{u}(\boldsymbol{r}) = \sum_{n=1}^{\infty} a_n \boldsymbol{s}_{n,m,\beta}(\boldsymbol{r}) \quad \text{with} \quad |a_n| < 1 \right\} \tag{67}$$

which can be imagined as a cube of volume 1. With R we compared the set of daughters

$$T: = \left\{ \boldsymbol{u}(\boldsymbol{r}) \,|\, \boldsymbol{u}(\boldsymbol{r}) = \sum_{l=1}^{\infty} \gamma_l \boldsymbol{h}_{c_l}(\boldsymbol{r}) \quad \text{with} \quad |\gamma_l| < 1 \right\}. \tag{68}$$

To calculate its volume, the Hagen functions were expanded in terms of Stokes functions, and the resulting transformation determinant was evaluated (consult Sect. 2.4 on the numerical techniques). In the frame of a simple model this kind of volume computation was explained in Section 4.2. But here we have a space of infinite dimension so that it seems as if the outcome should always depend on truncation. Nevertheless it appears that the procedure converges since the highly damped Hagen functions approach the Stokes functions, as discussed in connection with Figs. 14 and 15.

Volumes of T for several values of m, β, and Re are compiled in Figure 28. Consider first the line $\mathrm{Vol}(m = 1, \beta = 0.5)$ in Part a which displays the volume spanned by the $m = 1$, $\beta = 0.5$ Hagen functions. For $\mathrm{Re} = 0$,

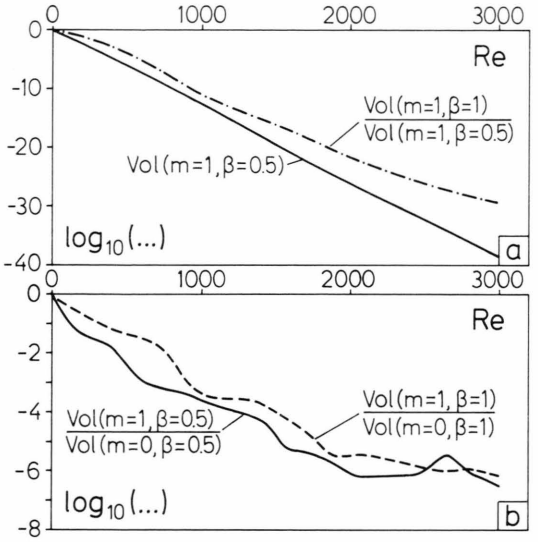

Fig. 28. Spaces of daughterhood. Shown are volumes or ratios of volumes of the set T as defined in (68). The ordinates measure decadic logarithms of the quantities.

Hagen and Stokes functions coincide; the volume must be 1. With increasing Reynolds number the volume gets smaller, evidently exponentially, and reaches for $\mathrm{Re} \approx 2000$ values as small as 10^{-25}. Since mothers fill the set $R - T$, it seems fair to claim that nearly all disturbances are mothers.

The $m = 0$ modes are unable to produce a sizable mother-daughter effect, as remarked in the Sections 4.1 and 4.3. Figure 28 b presents further evidence for this. Such ratios as $\mathrm{Vol}(m = 1,\ \beta = 0.5)/\mathrm{Vol}(m = 0,\ \beta = 0.5)$ exhibit that the $m = 1$ Hagen functions are much more defective than those with $m = 0$.

A similar ratio $\mathrm{Vol}(m = 1,\ \beta = 1.0)/\mathrm{Vol}(m = 1,\ \beta = 0.5)$ is shown in Figure 28 a. To appreciate the meaning of its steep decrease with Re, one has to remember the strange strength of the $\beta = 1.0$ modes documented in Figure 11. This strength is so surprising because the $\beta = 0.5$ modes should always get a better amplification (see Figure 13 b). But although $\beta = 1.0$ has the worse mothers, it lodges much more of them. And since the quality of the mothers varies linearly with the Reynolds number whereas their relative abundance grows exponentially, we understand now that short-wave disturbances are increasingly favored when the Reynolds number grows.

All questions asked at the end of Chapt. 3 are answered now.

5. Specialities of Non-linearity

Eventually we understand the double threshold: At small Reynolds numbers, only few mothers exist, and these produce just feeble daughters. Under such circumstances the non-linearity is inessential because it on its own cannot transfer energy to the disturbance. With growing Reynolds number the mothers get more and better. But if we start with a too small mother, then also her daughter remains too small to activate the nonlinear terms. The mother dies away then, the daughter remains a daughter, and the flow returns to laminarity. With this as the fundamental mechanism, it seems that knowledge concerning the non-linearity is less important. Nevertheless, some remarks on its traits must be made.

α) The non-linearity is a random mixer. We found evidence for this by studying systems with various non-linear parts. The common property of these systems is just the presence of mothers and daughters.

β) The non-linearity activates more than three degrees of freedom. It is thus essential for permanent turbulence that *collective defectiveness* takes place. In order words, one mother-daughter pair as discussed in Sect. 4.2 is not sufficient.

5.1 *Various Non-linearities in the Large System*

Using transverse functions (as the Stokes functions happen to be) one may derive immediately from the Navier-Stokes equation (2) a set of Galerkin equations. If one assumes (although it is wrong) that the pressure varies periodically, it drops out, as one can see by partial integration. The equations of motion have the same structure as those in (13) but rely on modified matrices:

$$\hat{W}_\mu^{\varkappa\lambda} = \int_{(\text{pipe})} \boldsymbol{s}_\mu^* (\boldsymbol{s}_\varkappa \times \boldsymbol{w}_\lambda)\, \mathrm{d}\tau, \tag{69}$$

$$\hat{H}_\mu^\varkappa = \int_{(\text{pipe})} \boldsymbol{s}_\mu^* (\boldsymbol{s}_\varkappa \times \boldsymbol{W}_{\text{HP}} + \boldsymbol{U}_{\text{HP}} \times \boldsymbol{w}_\varkappa)\, \mathrm{d}\tau, \tag{70}$$

$$\hat{D}_\mu^\varkappa = -\alpha_\mu^2\, \delta_\mu^\varkappa. \tag{71}$$

Except for $\hat{D}_\mu^\varkappa$, these matrices are not equivalent to those in (14)–(16). Using them (see e.g. [6, 33]) gives definitely worse approximations since this approach puts no constraints on the longitudinal part of (2). The system defined by (69)–(71) has nevertheless an advantage: The modified interaction matrix satisfies the symmetry property

$$(\hat{W}_\mu^{\varkappa(n_\lambda, m_\lambda, l_\lambda)})^* = -(-)^{m_\lambda}\, \hat{W}_\varkappa^{\mu(n_\lambda, -m_\lambda, -l_\lambda)}. \tag{72}$$

This follows from (69) and (A.16), and from a well-known identity of vector algebra. Combined with the reality condition (33), (72) shows that the modified interaction input according to (25) contributes nothing at all to the energy balance as specified in (28). The two interaction matrices (14) and (69) are therefore at least in one characteristic aspect different. In contrast, the modified Hagen matrix of (70) shares with the Hagen matrix of (15) common properties: It describes, together with the dissipation matrix, a system which is stable for all Reynolds numbers, and it has daughters and mothers even though eigenvalues and eigenfunctions are generally not the same as in the original system.

Numerical solution of the modified dynamical system exhibited very much the same characteristics as described in Chapt. 2, in particular a similar double threshold as in Fig. 2 was obtained. From this we concluded: First, the argument that small deviations of the interaction input W_{inp} from zero (displayed e.g. in the Figs. 6–9) might still be important, is decisively wrong. Second, the onset of chaos cannot depend on non-generic pecularities of the non-linear terms.

Even more striking evidence for the last point was discovered when we studied a 'constant-pressure' system. It is different from the 'constant-flux' system of Chapt. 3 by another expansion of the total velocity field

$$\boldsymbol{U}(\boldsymbol{r}, t) = a_0(t)\, \boldsymbol{U}_{\text{HP}}(r) + \sum_{\nu=1}^{N} a_\nu(t)\, \boldsymbol{s}_\nu(\boldsymbol{r}). \tag{73}$$

It has a non-constant Hagen-Poiseuille term (cf. (7)). The additional coefficient $a_0(t)$ was used to maintain a constant pressure drop on the pipe's axis, i.e. it was coerced to fulfil the requirement of a constant pressure drop at the pipe's center

$$-\frac{4}{\text{Re}}\, a_0(t) + \Delta p(r = 0, \mathrm{t}) = -\frac{4}{\text{Re}}. \tag{74}$$

The pressure drop caused by the disturbance $\Delta p(r = 0, \mathrm{t})$ alone was calculated from the amplitudes $a_\nu(t)$, $\nu = 1, 2, \ldots, N$ according to (3). The coefficient $a_0(t)$, which is due to (74) a non-linear function of the other amplitudes, appears again as a factor at the Hagen matrix in the equations of motion (13), and so it modifies the evolution. The flux is here, in difference to the pressure drop, not constant since we inserted in

Table 4. Stokes modes for the constant-pressure runs. The periodicity length was $L = 2\pi$, and hence $l = -1, 0, +1$ is equivalent to $\beta = -1, 0, +1$.

	$l=-1$	$l=0$	$l=+1$
$m=-1$	15	15	15
$m=0$	15	15	15
$m=+1$	15	15	15

(73) Stokes functions with the axial wave number $\beta = 0$. Table 4 presents a survey on all included Stokes modes.

As initial condition we chose

$$a_{1,\pm1,-1}(0) = a_{1,0,-1}(0) = (1+i)\,A_0,$$
$$a_{1,\pm1,0}(0) = (1+i)\,A_0,$$
$$\Re\, a_{1,0,0}(0) = A_0. \qquad (75)$$

The amplitudes for the modes with $m = 0, l = 0$, by the way, must be real as follows from the reality conditions (33).

The constant-pressure system exhibited again the double threshold although the constraint (74) introduces a qualitatively new kind of non-linearity. It is this point that we want to stress; the quality of the system as an approximation to reality is certainly not good enough (cf. Figure 29).

But we made also counterchecks: Systems with more blocks than in the Tables 1 or 4 were studied, including in particular the multipolarities $m = \pm 2$, taking all non-linear couplings into account, but keeping mothers and daughters out. The last condition was warranted as every single block was represented by one Stokes function only. In no case we observed anything like chaos; even no irregular transient was ever seen.

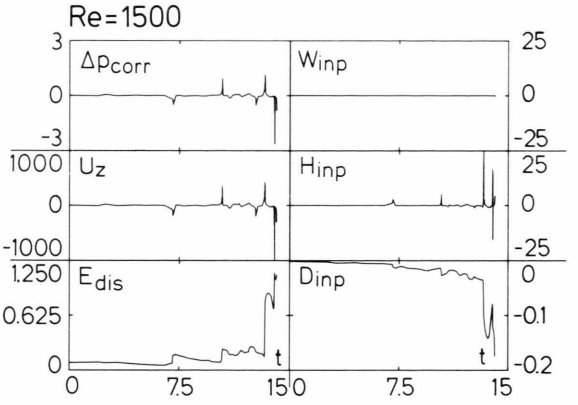

Fig. 29. A six-plot similar to Figs. 6 through 9 but for the constant-pressure system. In contrast to those figures, no pressure fluctuations can be shown. Δp_{corr} means just the correction of the pressure due to the disturbance which is necessary, according to (74), to achieve a constant total pressure. Compare the gigantic peaks of the velocity u_z with the peaceful behavior of the same quantity in the Figures 6–9.

5.2 *Search for Small Systems*

The arguments presented in the previous section do already suggest that pipe turbulence is essentially a system with many degrees of freedom: The non-linearity as a random mixer needs a high-dimensional phase space. To support this point of view, we looked for the dimension of the chaotic attractor, using the simplest Grassberger-Procaccia prescription [34], and found no indication for a fractal dimension smaller than three. This is similar as in recent experimental work by Sieber [35] done, however, at larger Reynolds numbers. But because of the insufficient statistics of our presently available data we cannot take this as evidence.

There is still another method to find the number of the essentially needed degrees of freedom: the search for a small system which has similar dynamical features. First we reduced the number of Stokes functions in every block (cf. Table 1) from 20 to 15 and detected no significant change in the phenomena. We could not go further on this way because further reduction provokes linear instability (see the italicized remark in Section 2.4). However, 180 essential degrees of freedom is established as an upper limit for the constant-flux systems of Chapter 3.

Then the number of essential degrees of freedom was approached from below by constructing small systems based on the following rules:

S1) A small system should have the same structure as the large system (13), i.e. it must consist of first-order ordinary differential equations which have only linear and quadratic terms on their right-hand sides; the analogs of the interaction and Hagen matrices must be purely imaginary, while the dissipation matrix must be real (cf. (14)–(16)).

S2) Amplification should be effected exclusively by the mother-daughter mechanism (cf. Chapter 4). Linear instability is not admissible.

S3) The non-linear terms should conserve energy (cf. Sects. 3.3 and 5.1).

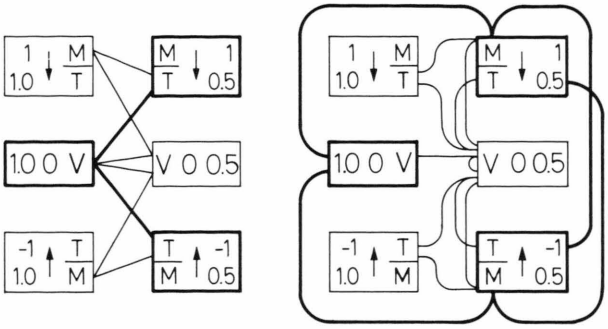

Fig. 30. Block diagram of the constant-flux system. To see all interactions together, one must overlay to two parts right and left. The $-\beta$ blocks are merged into the $+\beta$ blocks according to the reality condition (33). This one must not forget while checking the selection rules (17).

S4) The different m-l blocks as indicated in the Tables 1 and 4 must be represented and the selection rules (17) and (18) obeyed.

The implementation of these rules shall be now exemplified.

In Fig. 30 the complete dynamics as described by (13) and Table 1 is displayed. Consider first the blocks. Each of them represents a community of Stokes functions with fixed m (integer number) and $\beta = 2\pi l/L$ (real number). But the Stokes functions are just computational devices. The physical essentials are the mothers and the daughters; so they are distinguished as M and T in the blocks. The mothers procure energy for the daughters; this is what the arrows are to indicate. However, only the blocks with $m = \pm 1$ have mother-daughter features (cf. Section 4.1). Therefore it should be sufficient to design just one class of modes, the mediators V, for $m = 0$.

According to the selection rules (17), non-linear interaction within the blocks does not exist except for $m = 0$, $l = 0$. In Fig. 30 the non-linear couplings are depicted as lines which connect blocks. Here it is useful to discriminate between 'donors' and 'acceptors' which are defined as soon as the non-linear part of (13) is isolated: In the relation $d_t a_\mu(t) = W_\mu^{\varkappa\lambda}\, a_\varkappa(t)\, a_\lambda(t) + \ldots$ the amplitudes $a_\varkappa(t)$ and a_λ on the right-hand side are donors, while $a_\mu(t)$ on the left-hand side is an acceptor. Donors are identified in Fig. 30 as members of those blocks from which the connecting lines depart as singles. Two connecting lines join at the respective acceptor. It would be too confusing to draw all lines in one diagram. The blocks were therefore doubled, and in the left-hand part only those couplings were entered which act from $\beta = 0.5$ to $\beta = 1.0$, whereas the right-hand part was reserved for couplings in the opposite direction.

Due to the usually much greater intensity of the daughters (see Sect. 3.4), it seems sensible to use just daughters T as donors, and mothers M only as acceptors. The special role of the mediators V may be rated with the help of Fig. 30: Only by their participation regeneration of mothers is possible. The mediators, on the other hand, can be fed just by non-linear interactions. Therefore the mediators must be donors and acceptors at the same time.

The diagram in Fig. 30 is reducible in the sense that the complete family of all six blocks does not represent the smallest system in which the mother-daughter mechanism and non-linear interaction according to the selection rules can happen. The smallest system is set off by the heavy lines. For this we will continue the construction.

The formal composition is grossly simplified if the following division is recognized: linear interaction only within the blocks, non-linear couplings only between them; this is a trivial inference from the selection rules (17) and (18). For each of the $m = \pm 1$ blocks in the reduced scheme we allow only one daughter-mother pair, and we take it in its completely defective form as introduced in Sect. 4.2:

$$\begin{aligned} d_t T_{\pm 1}(t) &= (i h - d)\, T_{\pm 1}(t) + i g\, M_{\pm 1}(t), \\ d_t M_{\pm 1}(t) &= + (i h - d)\, M_{\pm 1}(t). \end{aligned} \tag{76}$$

The complex amplitudes $T_{\pm 1}(t)$ and $M_{\pm 1}(t)$ are assigned now to daughters and mothers as the $a_\nu(t)$ were assigned to the Stokes functions in (7). A discrimination with respect to β is here not necessary. Only two kinds of non-linear couplings may occur (cf. Fig. 30):

$$\begin{aligned} d_t M_{+1,0.5}(t) &= w_{\mathrm{M}}^{\mathrm{TV}}\, T_{+1,-0.5}(t)\, V_{0,1.0}(t), \\ d_t M_{-1,0.5}(t) &= w_{\mathrm{M}}^{\mathrm{TV}}\, T_{-1,-0.5}(t)\, V_{0,1.0}(t) \end{aligned} \tag{77}$$

and

$$d_t V_{0,1.0}(t) = w_{\mathrm{V}}^{\mathrm{TT}}\, T_{1,0.5}(t)\, T_{-1,0.5}(t). \tag{78}$$

This time both indices m and β were attached to demonstrate the fulfillment of the selection rules. However, comparing (78) with (77) one recognizes that this combination of non-linearities cannot conserve energy. The only way to warrant this is

$$\begin{aligned} d_t V_{0,1.0}(t) = w_{\mathrm{V}}^{\mathrm{TM}} &(T_{1,0.5}(t)\, M_{-1,0.5}(t) \\ &+ M_{1,0.5}(t)\, T_{-1,0.5}(t)), \end{aligned} \tag{78'}$$

i.e. for a certain purpose also mothers have to be admitted as donators. Since mediators, daughters, and mothers are just linear combinations of Stokes modes, they must satisfy the reality condition (33). This permits to eliminate from (77) the amplitudes with negative wave numbers. Furthermore, the rule S3 reduces the two coupling constants w_V^{TM} and w_M^{TV} to only one:

$$w_V^{TM} = -w_M^{TV} =: iw, \tag{79}$$

where w denotes now a real constant. When finally (76)–(79) are composed, the complete small system is obtained

$$\begin{aligned}
d_t T_{-1} &= (ih - d)\, T_{-1} + \quad ig\, M_{-1}, \\
d_t M_{-1} &= \quad + (ih - d)\, M_{-1} + iw\, T_{+1}^*\, V, \\
d_t V &= (ih_0 - d_0)\, V + iw(T_{+1}\, M_{-1} + M_{+1}\, T_{-1}), \\
d_t T_{+1} &= (ih - d)\, T_{+1} + \quad ig\, M_{+1}, \\
d_t M_{+1} &= \quad + (ih - d)\, M_{+1} + iw\, T_{-1}^*\, V.
\end{aligned} \tag{80}$$

These are 10 real equations of motion. For the constants we took $h = -0.6$, $d = -0.25$ (cf. the circle in Fig. 15) and $h_0 = -0.8$, $d_0 = -0.2$ since some Hagen functions with $m = 0$, $\beta = 1.0$ have at $\mathrm{Re} = 2000$ about this as phase velocity and smallest damping. The non-diagonality was given the value $g = -1$ to warrant sufficient amplification (see (59)). The system (80) was solved many times, each time with a different value of the coupling constant w or with different initial conditions. We found often irregular transients as that in Fig. 6, but never permanent chaos.

Afterwards we extended the system to represent all the blocks and connections depicted in Fig. 30 and added more coupling constants until we had 4 of them and 20 differential equations. We admitted, however, never more than one mother-daughter pair per block. In all these cases no permanent chaos was seen although the irregular transients lived longer in the more complex systems. Even if one disregards the freedom contained in the initial conditions, a four-dimensional parameter space had to be scanned. Therefore we cannot claim that nothing was overseen. Nevertheless we suggest that the number of relevant degrees of freedom is somewhere between 20 and 180 for the onset of turbulence in a pipe.

6. Hints to the Experimenters

The comparison with experiments in the Sect. 3.1 and 3.2 revealed that even elementary data for the transition to turbulence in a pipe are not available, despite of much useful experimental work (see e.g. the list of references in [36]). We are aware that such measurements are difficult since long-living transients may cause irreproducible records. Nevertheless we propose to establish a data set of average velocities and pressures as well as of their variances for $2000 < \mathrm{Re} < 3000$. We stress once more the importance of a complete pressure profile as given by us in Figure 4. And we urge the experimentalists to care for constant flux; otherwise there is danger that one observes properties of the environment rather than properties of the pipe.

A second task is a more precise identification of daughters. This can be done, for example, in a correlation experiment [25]: A strong change of pressure is originated, according to our theory, by a powerful daughter. Thus one should see, in correlation with a pressure burst, acceleration close to one side of the pipe accompanied with a retardation on the other side. Another characteristic property is the missing φ-component, visible in the reduced isotropy of the flow field.

Most appealing, however, are the mothers since 'ruling mothers means ruling turbulence'. To visualize these meek but allimportant flows, progress in experimental arts seems desirable.

α) One should be able to have a well-prepared Hagen-Poiseuille flow and to provoke at the same time *define disturbances*, e.g. disturbances with a chosen multipolarity and wavelength. We know of two methods:

αi) A part of the pipe can be made from a flexible material. Defined disturbances can thus be excited by deformations of the insert. The device should be completed by some apertures for sucking and injection since only a combination of deformation and injection may differentiate between daughters and mothers [37].

αii) Additives in the fluid can allow for an electric current. When moreover magnets are aptly installed around the pipe and suitably switched on and off, the wanted disturbance must arise [38].

It should be remembered that the experimental proof of the Tollmien-Schlichting instability was possible only after the introduction of defined disturbances [39]. Leite seems to have started the first and up to now most successful attempt to excite defined disturbances in a pipe [22]. He achieved this by putting obstacles of various shapes into the flow. The method is problematic because vortices are produced

directly behind the obstacle and have, because of symmetry breaking, usually a multipolarity different from that of the obstacle.

β) Turbulence, in particular onset of turbulence, is a generally three-dimensional phenomenon. The experimental techniques must be able to monitor three-dimensional structures as our Figs. 16–26 do. We think of crossed optical imaging plus a doubled video recording system to produce movie-like records. A time resolution of 1/10 sec should be good enough for the visualization of transitional turbulence of water in a pipe with 1 cm radius.

The further procedure is then straightforward: Similarly as we did with the initial conditions (36)–(39), the experimentalist produces various defined disturbances and observes the response. If a mother takes part, turbulence should arise with relative ease. Furthermore, it should be possible by these methods to construct analogs of our Fig. 2, that is to document the double threshold by quantitive measurements.

We wish to express our gratitude to S. Großmann for support and much useful advice.

Appendix: The Stokes Functions

Generalized Stokes functions were presented in [40]. We adapted the formulas given there to the special case needed for this work. Novel is the formula for the normalization (A.12).

A convenient way to compute solutions of the differential equation (9) is by the representation

$$\boldsymbol{s}(\boldsymbol{r}) = \boldsymbol{\nabla} \times a(\boldsymbol{r}) + \boldsymbol{\nabla} \times \boldsymbol{\nabla} \times b(\boldsymbol{r}) + \boldsymbol{\nabla} c(\boldsymbol{r}) \tag{A.1}$$

from the three potentials

$$\begin{aligned} a(\boldsymbol{r}) &= -A\, J_m(\gamma r)\ \ e^{i(m\varphi+\beta z)}, \\ b(\boldsymbol{r}) &= -B\, J_m(\gamma r)\ \ e^{i(m\varphi+\beta z)}, \\ c(\boldsymbol{r}) &= -C\, I_m(\beta r)\, i\, e^{i(m\varphi+\beta z)}, \end{aligned} \tag{A.2}$$

with constant factors A, B, C and the abbreviation $\gamma := \sqrt{\alpha^2 - \beta^2}$. Indices are avoided here as far as possible. The phases in (A.2) were chosed to make the functions $\boldsymbol{s}(\boldsymbol{r}) = \boldsymbol{S}(r)\, e^{i(m\varphi+\beta z)}$ (cf. (10)) as simple as possible: Evaluation of (A.1) with (A.2) gives

$$\boldsymbol{S}(r) = -i\,u(r)\,\boldsymbol{e}_r + v(r)\,\boldsymbol{e}_\varphi + w(r)\,\boldsymbol{e}_z \tag{A.3}$$

with tree real functions

$$\begin{aligned} u(r) &= A\left(\tfrac{m}{r} J_m(\gamma r)\right) + B(\beta\gamma J'_m(\gamma r)) + C(\beta I'_m(\beta r)), \\ v(r) &= A(\gamma J'_m(\gamma r)) + B\left(\tfrac{m\beta}{r} J_m(\gamma r)\right) + C\left(\tfrac{m}{r} I_m(\beta r)\right), \\ w(r) &= \qquad\qquad B(-\gamma^2 J_m(\gamma r)) + C(\beta I_m(\beta r)). \end{aligned} \tag{A.4}$$

$\boldsymbol{e}_r$, $\boldsymbol{e}_\varphi$, $\boldsymbol{e}_z$ are unit vectors in cylindrical coordinates, and $J_m(z)$ and $I_m(z)$ standard and modified Bessel functions, respectively. Primes are attached to indicate derivatives with respect to the argument. The pressure as defined in (9) is given by

$$p(\boldsymbol{r}) = -C(\alpha^2 I_m(\beta r))\, i\, e^{i(m\varphi+\beta z)}. \tag{A.5}$$

For evaluation of curls it is advisable rather to use the representation (A.1) and to remember that the Stokes functions obey

$$\alpha^2 \boldsymbol{\nabla} \times \boldsymbol{s}(\boldsymbol{r}) = \boldsymbol{\nabla} \times \boldsymbol{\nabla} \times \boldsymbol{\nabla} \times \boldsymbol{s}(\boldsymbol{r}) \tag{A.6}$$

than to operate with elementary differentiations on (A.3) and (A.4).

The boundary conditions (5) are fulfilled if the characteristic equation

$$\begin{aligned} \beta\gamma^2 J'_m(\gamma)(\beta J'_m(\gamma) I_m(\beta) + \gamma J_m(\gamma) I'_m(\beta)) \\ - m^2 \alpha^2 J_m^2(\gamma) I_m(\beta) = 0 \end{aligned} \tag{A.7}$$

is satisfied. From the characteristic equation one may compute γ or $\alpha^2 = \beta^2 + \gamma^2$ for any given m and β. However, (A.7) has even for fixed m and β an infinite series of zeros. Upper and lower bounds for these zeros can be found by the same procedure as in [5]:

$$z'_n < \gamma < z_n \quad \text{and} \quad z_n < \gamma < z'_{n+1}. \tag{A.8}$$

z_n and z'_n denote the n^{th} zeros ($n = 1, 2, 3, \ldots$) of the equations $J_m(z_n) = 0$ and $J'_m(z'_n) = 0$, respectively. We established that these estimates can be replaced by

$$\beta^2 + \left(\frac{n}{2} + \frac{1}{4}\right)^2 \pi^2 < \alpha^2 < \beta^2 + \left(\frac{n}{2} + \frac{3}{4}\right)^2 \pi^2$$

for $m = 0$ and

$$\begin{aligned} \beta^2 + \left(\frac{|m| + n}{2} - \frac{1}{4}\right)^2 \pi^2 \\ < \alpha^2 < \beta^2 + \left(\frac{|m| + n}{2} + \frac{3}{4}\right)^2 \pi^2 \end{aligned} \tag{A.9}$$

for $|m| = 1, 2, 3$, if $|\beta| < 8$.

After the solution of the characteristic equation one may compute the factors

$$\begin{aligned} A &= -B\, m\, \alpha^2 J_m(\gamma)/(\beta\gamma J'_m(\gamma)) \\ C &= \quad B\ \ \gamma^2 J_m(\gamma)/(\beta I_m(\beta)) \end{aligned} \tag{A.10}$$

for some fixed B. In the case $m = 0$, these formulas are not applicable for the odd zeros ($n = 1, 3, 5, \ldots$). There one has to choose a value for A and put $B = C = 0$. All this determines the functions $u(r)$, $v(r)$, and $w(r)$ up to a common factor. Absolute normalization is obtained from (11). The integrals in (11) can be evaluated with the following trick: Standard manipulations make from (9)

$$\int_{(\text{pipe})} \boldsymbol{s}_\mu^* \boldsymbol{s}_\nu \, \mathrm{d}\tau = \frac{1}{\alpha_\mu^2 - \alpha_\nu^2} \oint_{(\text{surface of pipe})} \boldsymbol{s}_\mu^* (\times \nabla \times \boldsymbol{s}_\nu - p_\nu) \, \mathrm{d}\boldsymbol{a}, \tag{A.11}$$

where it was already used that $\boldsymbol{s}_\nu(\boldsymbol{r})$ satisfies not only the differential equation (9) but also both boundary conditions (5) and (6). Assuming the same for $\boldsymbol{s}_\mu(\boldsymbol{r})$ yields a proof for the orthogonality of the Stokes functions. But we stipulated that $\boldsymbol{s}_\mu(\boldsymbol{r})$ should obey

i) the differential equation (9) (i.e. (A.1–6) remain valid),

ii) the boundary condition (6) (i.e. β is kept fixed), but not the boundary condition (5), meaning that α_μ^2 is not necessarily a solution of the characteristic equation. Therefore we were entitled to put

iii) $\alpha_\mu^2 = \alpha_\nu^2 + \varepsilon$, and we computed the right-hand side of (A.11) for $\varepsilon \to 0$. This gave with (A.4–5)

$$\frac{1}{2\pi L} \int_{(\text{pipe})} |\boldsymbol{s}_\nu|^2 \, \mathrm{d}\tau = A^2 \frac{\gamma^2 - m^2}{2} J_m^2(\gamma) + ABm\beta J_m^2(\gamma) + B^2 \left(\frac{\alpha^2 \gamma^2 (\beta^2 + m^2)}{2\beta^2} J_m^2(\gamma) + \alpha^2 \gamma J_m(\gamma) J_m'(\gamma) + \frac{\alpha^2 \gamma^2}{2} J_m'^2(\gamma) \right). \tag{A.12}$$

Finally we had to consider the behavior of the functions under inversion of m and β. First it follows from the characteristic equation (A.7) that α^2 does not depend on such a change. With a slight generalization of notation we can write this as

$$\alpha^2(-m, -\beta) = \alpha^2(m, \beta). \tag{A.13}$$

Next one finds for the factors A and C from (A.10)

$$A(-m, -\beta) = A(m, \beta)$$
$$\text{and} \quad C(-m, -\beta) = -C(m, \beta) \tag{A.14}$$

provided that the sign of B is kept fixed. These relations and (A.4) yield

$$\begin{aligned} u(r; -m, -\beta) &= -(-)^m u(r; m, \beta), \\ v(r; -m, -\beta) &= \quad (-)^m v(r; m, \beta), \\ w(r; -m, -\beta) &= \quad (-)^m w(r; m, \beta). \end{aligned} \tag{A.15}$$

Knowledge of the elementary properties of Bessel functions suffices for the proof of (A.13–15). Putting (A.15) into (A.3) and returning via (10) to the Stokes functions and standard notation gives

$$\boldsymbol{s}_{n,-m,-l}(\boldsymbol{r}) = (-)^m \boldsymbol{s}_{n,m,l}^*(\boldsymbol{r}). \tag{A.16}$$

This formula is needed when one derives the conditions (33) for the reality of the expansion (7).

To obtain the formulas for $\beta = 0$, one may take the relations given in this Appendix, but must perform a limiting transition $\beta \to 0$.

[1] G. Hagen, Pogg. Ann. **46,** 423 (1839), and O. Reynolds, Phil. Trans. Roy Soc. **174,** 935 (1883).
[2] P. G. Drazin and W. H. Reid, Hydrodynamic Stability, Cambridge University Press 1981, Section 48.
[3] S. A. Orszag and A. T. Patera, Phys. Rev. Lett. **45,** 989 (1980).
[4] M. Lessen, S. G. Sadler, and T. Y. Liu, Phys. Fluids **11,** 1404 (1968).
[5] D. M. Burridge and P. G. Drazin, Phys. Fluids **12,** 264 (1969).
[6] H. Salwen, F. W. Cotton, and C. E. Grosch, J. Fluid Mech. **98,** 273 (1980).
[7] A. Davey and H. P. F. Nguyen, J. Fluid Mech. **45,** 701 (1971).
[8] P. K. Sen, D. Venkateswarlu, and S. Maji, J. Fluid Mech. **158,** 289 (1985).
[9] N. Itoh, J. Fluid Mech. **82,** 469 (1977).
[10] A. T. Patera and S. A. Orszag, J. Fluid Mech. **112,** 467 (1981).
[11] F. T. Smith and R. J. Bodonyi, Proc. Roy. Soc. London **A 384,** 463 (1982).
[12] H. Schlichting, Grenzschicht-Theorie, Braun-Verlag Karlsruhe 1982
[13] W. Gentzsch, Vectorization of Computer Programs with Applications to Computational Fluid Dynamics, Verlag Vieweg, Braunschweig 1984.
[14] W. H. Press, B. P. Flannery, S. A. Teukolsky, and W. T. Vetterling, Numerical Recipes, Cambridge University Press 1986.
[15] Å. Björck and G. Dahlquist, Numerische Methoden, Oldenbourg Verlag München 1979, p. 171.
[16] J. Stoer and R. Bulirsch, Introduction to Numerical Analysis, Springer-Verlag New York 1980.
[17] E. Fehlberg, Computing **6,** 61 (1970), method of Tab. 4.
[18] G. Bader and P. Deuflhard, A semi-implicit mid-point rule for stiff systems of ordinary differential equations, Report Sonderforschungsbereich 123, Heidelberg 1981.

[19] J. A. Nelder and R. Mead, Computer Journal **7,** 308 (1965).
[20] L. Boberg, Rechnungen zum Strömungswiderstand im Rohr bei zunehmendem Durchfluß, Diploma' Thesis, Philipps-Universität Marburg 1988.
[21] H. Salwen and C. E. Grosch, J. Fluid Mech. **54,** 93 (1972).
[22] R. J. Leite, J. Fluid Mech. **5,** 81 (1959).
[23] I. J. Wygnanski and F. H. Champagne, F. Fluid Mech. **59,** 281 (1973).
[24] A. Dinkelacker, private communication 1988.
[25] M. van Dyke, An Album of Fluid Motion, The Parabolic Press, Stanford 1982.
[26] J. Laufer, NACA report **1174,** (1954).
[27] A. P. de Iribarne, R. L. Hummel, J. W. Smith, and F. Frantisak, Chem. Eng. Prog. Symp. Ser. **65,** 60, (1969).
[28] A. S. Monin and A. M. Yaglom, Statistical Fluid Mechanics, Vol. 1 and 2, The MIT Press, Cambridge and London 1965.
[29] J. Meseth, Mitteilungen aus dem MPI für Strömungsforschung Göttingen **58** (1974).
[30] J. Meseth, Arch. Mech. **26,** 391 (1974).
[31] R. Zurmühl, Matrizen, Springer-Verlag, Berlin 1964, Kap. 5.
[32] J. H. Wilkinson, The Algebraic Eigenvalue Problem, Oxford University Press 1965.
[33] A. Leonard and A. Wray, in Lecture Notes in Physics (eds. H. Araki et al.), vol. 170, Springer Verlag Berlin 1982, p. 335.
[34] P. Grassberger and I. Procaccia, Physica **9d,** 189 (1983).
[35] M. Sieber, Mitteilungen aus dem MPI für Strömungsforschung Göttingen **83** (1987).
[36] I. J. Wygnanski, M. Sokolov, and D. Friedman, J. Fluid Mech. **69,** 283 (1975).
[37] G. E. A. Meier, private communication 1987.
[38] J. Heber, private communication 1987.
[39] G. B. Schubauer and H. K. Skramstad, J. Aeronaut. Sci. **14,** 69 (1947).
[40] U. Brosa, Z. Naturforsch. **41a,** 1141 (1986).